.

Highlights

Phase-field modelling of a liquid/liquid immiscible displacement through a network of capillaries

A. Vorobev,S. Prokopev,T. Lyubimova

- GPU algorithm for numerical modelling of multi-phase flows
- Direct calculation of capillary pressure for a complex interface in a micro-matrix
- Displacement flows in a single capillary and in uniform matrices occur qualitatively similarly
- Integral parameters quickly converge upon increase of the matrix size
- Capillary pressure is given by the difference of the flow rates for the two-phase and single-phase flows

Phase-field modelling of a liquid/liquid immiscible displacement through a network of capillaries

A. Vorobev[a,*], S. Prokopev[b] and T. Lyubimova[b,c]

[a] *Faculty of Engineering and Physical Sciences, University of Southampton, SO17 1BJ, UK*
[b] *Institute of Continuous Media Mechanics, UrB RAS, Perm, 614013, Russia*
[c] *Perm State University, Perm, 614990, Russia*

ARTICLE INFO

Keywords:
porous medium
capillary pressure
pore-level modelling
phase-field (Cahn-Hilliard) approach
GPU calculations

ABSTRACT

The liquid/liquid displacement through a 2D uniform network of capillaries is numerically modelled with the use of the phase-field approach. The detailed structure of the flow fields within the uniform matrices of different sizes (with the different number of pores) is examined with the aim to reveal the asymptotic behaviour, pertinent for a sufficiently large matrix, that could be used for representation of a porous medium. The integral characteristics of the flow that do not depend on the matrix size can be used for calculation of the parameters of a macroscopic (Darcy) approach. We demonstrate that qualitatively the displacement occurs very similarly in the matrices with the different number of structural elements. In particular, we show that the capillary pressure remains nearly constant during the displacement run until the break-through time (with some minor variations related to a particular shape of a matrix). Upon increase of the matrix size the magnitude of the capillary pressure (and all other integral characteristics of the two-phase flow) quickly converge to the limiting value (so that the limiting results are already reached for a matrix with 6×6 elements), giving the direct procedure for calculation of the capillary pressure in a porous medium.

1. Introduction

1.1. Continuous and pore-level descriptions of multiphase flows in a porous medium

We develop a theoretical model for accurate description of a liquid/liquid displacement in a porous medium, i.e. assuming that the liquid that initially saturates a porous medium is being displaced by injection of another liquid. Numerous processes in nature and industry can be reduced to this physical configuration, including oil recovery, and the aquifer and soil remediations.

A traditional practical macroscopic description of a liquid/liquid displacement in a porous medium is given in the framework of an extended Darcy model (see e.g. Barenblatt, Patzek and Silin, 2003; Niessner, Berg and Hassanizadeh, 2011). The Darcy theory introduces such parameters as the relative permeabilities and the capillary pressure, that depend on the relative amounts of liquids in a porous matrix, and on many other properties of the solid matrix and liquids, such as the surface tension coefficient, wetting properties, geometry of the matrix, etc. Essentially, this means that the macroscopic (Darcy) theory incorporates not three but (infinite) number of phenomenological constants, as the experimental determination of the functions (or curves) of the relative permeabilities and capillary pressure requires the series of measurements of these phenomenological quantities for a (large) number of saturation levels. The data obtained via these measurements remain applicable only to a particular solid matrix and to a particular fluid mixture, making the numerical results produced with the use of the Darcy model site-, fluids-, and history-specific.

For a more universal understanding of multiphase flows in a porous medium the more fundamental analysis based on a pore-level scale is needed. There are different pore-level representations for porous matrices, with the different levels of details. The simplest model is a 'bundle of tubes' model that represent a porous medium by a set of parallel capillaries of different radii (Barley and Ruth, 2001). In our work we use a more advanced model called the network approach (see e.g. Aker, Maloy, Hansen and Batrouni, 1998) that represents a porous matrix by a network of pores and capillaries. We consider a relatively simple uniform arrangement of the pores and capillaries, although the consideration of much more complex arrangements built up with the use of CT-scanners can be found in the literature (see e.g.

*Corresponding author
A.Vorobev@soton.ac.uk (A. Vorobev)
ORCID(s): 0000-0001-7511-2910 (A. Vorobev); 0000-0002-8212-2890 (T. Lyubimova)

Raeini, Bijeljic and Blunt, 2018).

Obviously, an increase in the complexity and size of a matrix is achieved by simplification of the models for the fluid flows. For instance, reproduction of some advanced features of the porous medium, such as heterogeneity, requires more than a million of structural elements in a matrix (Oren and Bakke, 2003), and modelling of multiphase flows in so large matrices could be only done using the percolation-type model, i.e. pre-setting the shapes of menisci in capillaries (e.g. Khaz'ali and Moghadasi, 2019). We however aim to resolve the shape of interfaces in a matrix, similarly e.g. to works by Huang, Meakin and Liu (2005); Prodanovic and Bryant (2006); Raeini, Blunt and Bijeljic (2012); Wang, Do-Duang and Amberg (2016); Shams, Raeini, Blunt and Bijeljic (2018) who model the multiphase flow through a single pore, a single capillary (micro-channel) with smooth and rough walls, and in a 'Y'-shaped capillary channel on the basis of the level-set, volume-of-fluid and phase-field methods. We consider a larger volume of the porous medium that incorporates many pores aiming to understand how the features of the fluid flow depend on the matrix size in order to deduce the asymptotic dependences of the integral characteristics that will not depend on the matrix size.

The data to be generated on the basis of pore-level simulations would be always excessive for practical users, who want the pore-level results to be upscaled onto a more practically-relevant continuous scale. Upscalling of the pore-level results can be obtained by analytical integration (volume averaging) of the microscopic equations over a representative element of the porous matrix (see e.g. Hornug, 1997). Obviously, owing to complexity of the approach, it would involve numerous difficulties and assumptions needed e.g. to solve the problem of averaging of the shapes of contact lines over complex geometry of a matrix or the problem of defining the macroscopic pressure (Hassanizadeh and Gray, 1993; Gray and Hassanizadeh, 1998; Nordbotten, Celia, Dahle and Hassanizadeh, 2008; McClure, Armstrong, Berrill, Schluter, Berg, Gray and Miller, 2018). Similar studies even involve homogenization (averaging) of the Cahn-Hilliard equations for the two-phase media (Papatzacos, 2002). Despite a significant impact of these models on our general understanding of the pore-level physics, the resultant averaged equations are rarely used for practical calculations, seemingly because the equations remain too complex (in comparison with the straightforward Darcy theory), with new non-traditional phenomenological parameters, with values unavailable for practical users.

An upscaling of the pore-level modelling can be also achieved through numerical calculation of the integral flow characteristics that can be used to determine the relative permeabilities and capillary pressure for a representative volume of the porous matrix, very similar to the way as if these parameters had been obtained from a physical laboratory experiment, e.g. using an approach similar to the one suggested by Li, Shen and Qing (1994). The pore-level calculation of the full hydrodynamic problem is however a highly computationally demanding task due to necessity to trace the dynamics of the interfacial line, and due to a complex geometry of the problem. This substantially limits the size of a volume of the porous medium that can be accurately modelled. The characteristics obtained for smaller matrices may happen to be dependent on the matrix size. In our study we aim to understand what is the minimum volume of a porous matrix, when the integral parameters of the fluid flow become size-independent, and thus may be used for calculation of the parameters of the continuous approach.

1.2. Capillary pressure

The current work focuses on calculation of the capillary pressure. The capillary pressure strongly affects the static distributions of phases and the dynamics of multiphase flows in a porous matrix. Owing to capillary action, a wetting phase easily penetrates into a porous matrix even against gravity (the spontaneous imbibition) and forms an irreducible content in a porous matrix; while penetration of a non-wetting phase into a porous matrix is only possible if the imposed pressure difference exceeds the capillary pressure. Owing to capillary trapping, a sponge immersed in water and then taken out remains water-saturated: water, despite being heavier than air, remains entrapped in a porous matrix of a sponge by capillary forces. The same effect helps plants to remain hydrated, complicates oil recovery or aquifer remediation, secures storage of liquid waste in porous media, and controls many other processes in nature and industry (see e.g. de Gennes, Brochard-Wyart and Quere, 2004).

How to calculate the capillary pressure associated with a static liquid/liquid meniscus within a single capillary is relatively clear. For instance, for an axisymmetric meniscus the capillary pressure is given by a classical formula (de Gennes et al., 2004),

$$p_c = \frac{2\sigma_* \cos\theta}{R}, \tag{1}$$

where σ_* is the surface tension coefficient, θ is the apparent contact angle, and R is the radius of the capillary. It is less clear how to calculate the capillary pressure for a non-axisymmetric meniscus, or for an interface that separates two

liquids within a complex arrangement of pores that represent the porous medium. For instance, one of the averaged approaches for two-phase flows in porous media develops a geometric description of the capillary pressure calculating the average mean curvature (McClure et al., 2018).

On the basis of the dimensional analysis, Leverett (1941) suggested calculating the capillary pressure in a porous matrix by using the formula

$$p_c = \sqrt{\frac{\phi}{k}}\sigma_* \boldsymbol{J}(s)\cos\theta. \tag{2}$$

Here ϕ and k are the porosity and permeability of a matrix, and $\boldsymbol{J}(s)$ is the so-called 'Leverett $\boldsymbol{J}$-function' of saturation (volume fraction), s, of one of the components in a liquid/liquid mixture that fills in the matrix. The idea was to come up with the universal $\boldsymbol{J}$-function that depends only on saturation, as the other properties of the matrix and liquids are already included in formula (2). This approach however failed to get an experimental validation. It was found that the $\boldsymbol{J}$-function remains to be quite different for different matrices and liquids. Nevertheless, formula (2) is still widely used for theoretical analyses, giving a clear and easy way to estimate the value of the capillary pressure.

An additional complexity in calculation of the capillary pressure in a porous media is introduced by its hysteresis (dependence on the history of the process) (Hassanizadeh and Gray, 1993; McClure et al., 2018). In addition, the contact angle and the capillary pressure change when the meniscus moves (i.e. depend on the flow rate) (see e.g. Kafka and Dussan V., 1979; Ngan and Dussan V., 1982; Prokopev, Vorobev and Lyubimova, 2019). In the current paper we demonstrate a procedure for exact calculation of the dynamic capillary pressure for a uniform $2\boldsymbol{D}$ network of capillaries.

2. Problem statement

2.1. Mathematical model. Phase-field approach

Within the phase-field approach the system of two liquids is represented as a heterogeneous binary mixture. The position of an interface is traced through the field of concentration, that is defined as the mass fraction of one of the liquids in a liquid/liquid mixture. A single set of the governing equations is written for the entire multiphase system, including the interface boundary, that is represented as a transitional layer of a finite thickness (across the boundary all variables experience sharp but continuous changes). To take into account the surface tension effects existent at interfaces, the free energy function of a mixture is redefined as follows (Cahn and Hilliard, 1959),

$$f(\boldsymbol{C}, \nabla\boldsymbol{C}) = f_0(\boldsymbol{C}) + \frac{\epsilon}{2}(\nabla\boldsymbol{C})^2. \tag{3}$$

Here f is the total specific free energy function and f_0 is its classical part (that do not include the surface tension effects). The magnitude of the additional term is given by the capillary constant ϵ, that is assumed to be so small that this term is negligible everywhere except for the places of very strong concentration gradients that correspond to interfaces.

The equations that determine the evolution of a heterogeneous binary mixture with the states given by the free energy function (3) are called the Cahn-Hilliard-Navier-Stokes equations (Lowengrub and Truskinovsky, 1998). The full equations although are rather difficult for numerical treatment, with the main difficulty caused by the effect of quasi-compressibility (the continuity equation needs to be used in the full form owing to dependence of the mixture density on concentration). In almost all works (see e.g. Jacqmin, 1999; Ding, Spelt and Shu, 2007; Ahmadlouydarab and Feng, 2014), the numerical solution is given in the framework of the Boussinesq approximation of the full equations. The Boussinesq approximation of the Cahn-Hilliard-Navier-Stokes equations was strictly derived in the works by Vorobev (2010); Vorobev and Lyubimova (2019), and this set of equations is employed in the current study.[1]

The governing equations include the laws of conservation for momentum, species, and mass:

$$\frac{\partial \boldsymbol{u}}{\partial t} + (\boldsymbol{u}\cdot\nabla)\,\boldsymbol{u} = -\nabla\Pi + \frac{1}{Re}\nabla^2\boldsymbol{u} - \frac{1}{M}C\nabla\mu, \tag{4}$$

[1] Other works postulate rather than derive the Boussinesq form of the full equations. There are some (minor) differences between the equations used in this work and the equations used by Jacqmin (1999); Ding et al. (2007); Ahmadlouydarab and Feng (2014). These differences are insignificant for description of immiscible liquids.

$$\frac{\partial C}{\partial t} + (\boldsymbol{u} \cdot \nabla) C = \frac{1}{Pe} \nabla^2 \mu, \tag{5}$$

$$\nabla \cdot \boldsymbol{u} = 0. \tag{6}$$

Here t is the time and $\boldsymbol{u}$ is the velocity vector (the velocity is defined as the mass-averaged velocity of a fluid particle that includes two components of a mixture). The quantity Π stands for the modified pressure that needs to be determined through the incompressibility constraint. The real pressure is given by the following expression,

$$p = \Pi - \frac{1}{M} \left(Cn \frac{(\nabla C)^2}{2} - \mu C + f_0 \right). \tag{7}$$

One sees that the right-hand side of equation (4) includes an additional term that is frequently called the Korteweg force. This term determines the action of the capillary forces that define the shape of an interfacial boundary. In the equation for the species balance (5) the diffusion term is given by the generalised Fick's law, that defines the diffusion flux proportional to the gradient of the chemical potential (Landau and Lifshitz, 1987). The chemical potential μ is set by the expression,

$$\mu = \frac{d f_0}{dC} - Cn \Delta C. \tag{8}$$

Equations (4)-(8) are written in the non-dimensional form. The following quantities, h, V_*, h/V_*, $\rho_* V_*^2$, μ_*, are chosen as the scales of length, velocity, time, pressure, and chemical potential. Here h is the diameter of a pore/capillary, V_* is the typical velocity, and μ_* and ρ_* are the typical values of the chemical potential and density.

The governing equations include the Reynolds, Peclet, Mach and Cahn numbers,

$$Re = \frac{\rho_* V_* h}{\eta_*}, \; Pe = \frac{\rho_* V_* h}{\alpha \mu_*}, \; M = \frac{V_*^2}{\mu_*}, \; Cn = \frac{\epsilon}{\mu_* h^2}. \tag{9}$$

The Reynolds number defines the ratio between the inertia and viscous forces. For flows in a porous medium the primary interest is given by the limit of low Reynolds numbers when the inertia terms are negligible (although, in some porous media, e.g. in fixed beds of chemical reactors, the Reynolds numbers may be as high as 1000 (see Wooding and Morel-Seytoux, 1976)).

The Peclet number determines the role of diffusion effects. Considerable smearing of an initially sharp interface should occur after a time period of the order, $\tau_d \sim Pe$. In the current study we focus on the dynamics of immiscible displacement, and thus we assume that $Pe >> 1$, or, in other words, the time needed for a liquid/liquid meniscus to move through a single element of the porous matrix is assumed to be much smaller than $\tau_d \sim Pe$.

The Mach number determines the strength of capillary effects in the Navier-Stokes equation. Namely, the surface tension coefficient (scaled by $\rho_* V_* h$) is given by the formula (Lowengrub and Truskinovsky, 1998; Prokopev et al., 2019),

$$\sigma = \frac{Cn}{MS} \int (\nabla C)^2 dV. \tag{10}$$

Here S is the area of the interface.

Finally, the Cahn number also determines the thickness of the liquid/liquid interface, as $\delta = \sqrt{2Cn}$ (Lowengrub and Truskinovsky, 1998; Vorobev, 2010).

It should be noted that the set of equations (4)-(6) assumes that two liquids of a mixture are characterised by similar viscosity coefficients. For derivation of these equations, it was assumed that the viscosity coefficients of the liquids are different, but the difference is small, so the leading term of the viscous force, that is kept in the equations, includes just one single parameter, that may be defined as the average viscosity of two liquids (see Vorobev, 2010; Vorobev and Lyubimova, 2019).

Finally, we need to define the expression for the classical free energy function, f_0, that determines the equilibrium states of a binary mixture (with omission of capillary effects). We are interested in the dynamics of a pair of immiscible liquids, which thermodynamic behaviour can be effectively represented by the so-called double-well potential (see e.g. Jacqmin, 1999; Ding et al., 2007; Ahmadlouydarab and Feng, 2014), that can be written as

$$f_0 = -\frac{1}{2}C^2 + C^4. \tag{11}$$

This expression has two minima, $\pm\frac{1}{2}$, that correspond to two components of the binary mixture.

2.2. Typical values of the parameters

The full problem (4)-(6) is determined by four governing parameters (9). The difficulty of the phase-field approach is in the use of the non-standard phenomenological coefficients, which values are not directly measurable. In particular, the definitions of the non-dimensional parameters (9) involve the typical value of the chemical potential, μ_*, the capillary constant ϵ, and the mobility coefficient, α.

In this work, we are primarily interested in the use of the phase-field method as a numerical tool for modelling the dynamics of immiscible sharp-interfaces. It is known that the thickness of a real immiscible interface is equal to just several molecular layers, $\delta_* \sim 1nm$ (see e.g. Jacqmin, 2000), which is zero for a macroscopic theory, and which is obviously a far too small length to be resolved in our simulations. For the sake of numerical solution, the interface is smeared, represented by a transitional layer of a finite thickness. In particular, in the phase-field approach the thickness of an equilibrium interfacial zone (scaled by the pore size h) is given by $\delta \sim \sqrt{2Cn}$ (see e.g. Lowengrub and Truskinovsky, 1998; Kheniene and Vorobev, 2013). The correlation of the real and modelling thicknesses suggests that the value of the Cahn number needs to be of the order, $Cn \sim 10^{-10}$ (for a pore size $h \sim 10^{-4}m$). In our simulations, although, much larger values of the Cahn number are used, and in order to reveal the physically relevant results, we perform the numerical simulations for the different Cahn numbers, taking values of the Cahn number gradually smaller, to establish the limiting behaviour of a system when the Cahn number tends to zero.

For a sharp interface, the concentration gradient has a non-zero value just within the interfacial zone, where its value is approximately equal to $1/\delta^2$. For a sharp interface, the integration in formula (10) gives the volume of the transitional zone as δS, which could be used to simplify the expression for the surface tension coefficient, as $\sigma \sim Cn/(M\delta)$, and additionally taking into account that the interface thickness is $\delta = \sqrt{2Cn}$, we conclude that the surface tension coefficient of a sharp interface is defined by,

$$\sigma \sim \frac{\sqrt{Cn}}{M}. \tag{12}$$

Following the work by Lowengrub and Truskinovsky (1998), for convenience, we introduce an additional parameter, $\gamma = \sqrt{Cn}/M$.

To retrieve the numerical results in the limit of a sharp interface, $\delta \to 0$, one needs to consider the smaller values of the Cahn number, as $\delta = \sqrt{2Cn}$. Formula (12) although indicates that the change of the Cahn number alters the surface tension coefficient. To keep the surface tension coefficient fixed, both parameters, Cn and M, need to tend to zero. In other words, for the phase-field simulations, the actual values of the Cahn and Mach numbers are unimportant. These are two technical parameters that are primarily introduced for the sake of numerical treatment. The numerical simulations are performed for the different values of these parameters, with the aim to establish the behaviour of a multiphase system in the limit when both Cn and M tend to zero (keeping the surface tension coefficient $\sigma \sim \gamma = \sqrt{Cn}/M$ fixed). This result reveals a physically-relevant behaviour of a multiphase system, even if the Cahn and Mach numbers remain different from their 'real' values.

Let us also estimate the expected role of the capillary forces for the displacement flows. For oil recovery applications, a typical pressure gradient can be estimated as $\Delta p/L \sim 10^7 Pa/10^3 m = 10^4 Pa/m$. Roughly, the imposed pressure difference on the scale of a pore can be estimated as $(\Delta p)_1 \sim (\Delta p/L)h \sim 1Pa$, while the estimates of the capillary pressure are much larger, $p_c \sim \sigma_*/h \sim 100Pa$ (for $\sigma_* \sim 10^{-2} N/m$, which is a typical value of the surface tension coefficient for an immiscible interface).

It should be however added that under subsurface condition, both water and oil absorb gases, which reduces the value of the surface tension coefficient. The absorption rates primarily depend on pressure (on the reservoir depth),

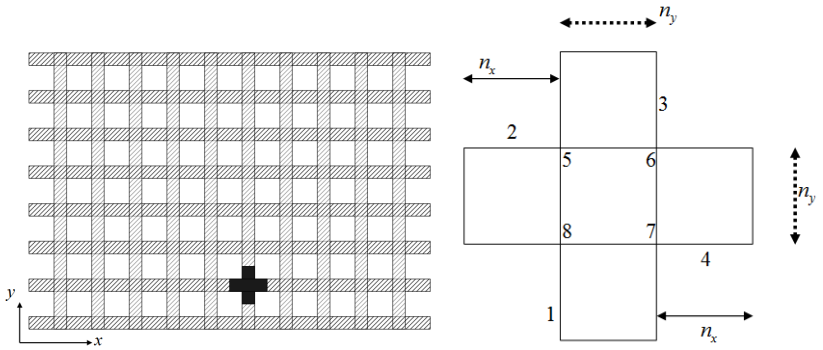

Figure 1: The overall geometry of the problem: the grey-shaded space corresponds to the voids of the matrix and the white space is the solids. The left and right ends of the matrix are open, and the top and bottom ends are closed. Injection of a liquid occurs at the left side of the matrix. A black cross is a base element of the matrix. (b) A detailed diagram of the base element of the porous matrix is shown at the left.

and the surface tension coefficient of oil/water interface might become as low as $10^{-3}N/m$. The surface tension coefficient is even lower (close to zero) for miscible interfaces (Vorobev, 2014). It should be added that the estimate for the capillary pressure and its role on the overall flow would strongly depend on the wetting conditions. If the displaced fluid is a wetting phase (and the displacing fluid is a non-wetting phase), then the displacement of such a fluid by the considered pressure differences seems to be impossible. In the opposite case, when the displacing fluid is a wetting phase, its motion into the porous matrix is primarily driven by the capillary effect, while the role of the imposed pressure difference is insignificant. In our work, we focus on the consideration of the neutral wetting conditions, when the equilibrium contact angle equals to 90^0. This does not negate the capillary effect, since the capillary pressure is determined by the dynamic contact angle that is the function of the flow rate (i.e. the imposed pressure difference), and that is generally different from its equilibrium value (Kafka and Dussan V., 1979; Ngan and Dussan V., 1982; Prokopev et al., 2019). Nevertheless, the accepted wetting condition makes the capillary pressure much smaller than an estimate, σ_*/h.

Next, we estimate the value of the Reynolds number, which definition is based on the parameters of a single pore/capillary. The maximum velocity of the fluid flow in a single capillary is given by the following equation,

$$V_{max} = \frac{\Delta p}{L}\frac{h^2}{8\eta_*}. \tag{13}$$

In our study we use this value as the velocity scale, $V_* = V_{max}$. If one assumes that the mixture that saturates a capillary has the viscosity coefficient $\eta_* \sim 10^{-3}Pa \cdot s$ and density $\rho_* \sim 10^3 kg/m$, then for a capillary of the diameter $h \sim 10^{-4}m$, the typical value of velocity is $V_* \sim 10^{-2}m/s$. In this case, the Reynolds number can be estimated as $Re \sim 1$. For interpretation of the numerical results, it would be also useful to know the value of the time scale, $\tau \sim 0.01s$. In addition, for a sharp immiscible interface, the non-dimensional value of the surface tension coefficient remains time-independent, and its value can be estimated as $\sigma = \sigma_*/(\rho_* V_* h) \sim 10^3$ (for $\sigma_* \sim 10^{-2}N/m$).

Finally, the value of the mobility coefficient can be calculated as $\alpha \sim \rho_* D_*/\mu_*$ (where D_* is the diffusion coefficient). We are interested in the dynamics of immiscible interfaces, when diffusive processes remain insignificant, making the mobility coefficient and the Peclet number rather technical parameters. We assume that the Peclet number is sufficiently high for the diffusion time-scale, $\tau_d \sim Pe$, to be much greater than the duration of an overall evolution of a multiphase system in a matrix. The actual value of the Peclet number can be determined by using equation, $Pe = V_* h/D_*$.

2.3. Geometry and boundary conditions

The geometry of the problem is depicted in figure 1a. Namely, we model the fluid flow within a $2D$ matrix that is built up by a repetition of a base element (a cross) along the horizontal (x) and vertical (y) directions. The base element of the matrix (a cross) may be further split into five more elementary squares/rectangles (see figure 1b). Two spatial sizes that define the base element are given by the spatial step h_1 and by the numbers of the nodes, n_x and n_y,

along the sides, as shown in figure 1b. The product of n_y and the spatial step h_1 is always equal to the unit length. At the ends of the matrix, some parts of the crosses are cut off as can be seen in figure 1a.

The porosity of the modelled matrix (with the unit element (cross) repeated M_x and M_y times in the x and y directions, respectively) is given by the expression,

$$\phi = \frac{M_y(4n_xn_y + n_y^2) - 2n_xn_y}{M_y(2n_x + n_y)^2 - 2n_x(2n_x + n_y)}. \tag{14}$$

For a large matrix, when $M_y \to \infty$, and when $n_x = n_y$, the porosity of the matrix would tend to $5/9$, which is quite large value, non-typical for real porous matrices. The values of the porosity seem to be more realistic when the lengths of the connecting capillaries are longer then the sizes (widths) of pores, which can be controlled by taking the ratio $n_x/n_y > 1$.

We assume that initially, the void space of the matrix is filled with the liquid that is defined by the concentration level $C = 1/2$. The pressure and the chemical potential are uniform, $p = 0$ and $\mu = 0$. The liquid is motionless, $\boldsymbol{u} = 0$.

To induce the flow through the matrix, the pressure difference between the left and right ends of the matrix is imposed. Namely, at the left side of the matrix, at all openings, the following boundary conditions are imposed:

$$p = p_1 \equiv \frac{8L_x}{Re}, u_y = 0, C = -\frac{1}{2}, \mu = 0. \tag{15}$$

Here, L_x is the horizontal size of the matrix. The pressure level, p_1, set at the inlet boundary is chosen so that the maximum value of the velocity in a single capillary (the velocity at the centreline) is equal to 1 for a single-phase flow. The boundary condition for the concentration field implies that the injected liquid differs from the liquid that initially saturates the matrix.

At the outlet end of the matrix, at all openings, the boundary conditions are

$$p = p_2 = 0, u_y = 0, \frac{\partial C}{\partial x} = 0, \mu = 0. \tag{16}$$

Here it is assumed that the ejected phase remains continuous at the outlet.

Finally, at the rigid walls of the flow pathways the imposed boundary conditions are

$$u_x = u_y = 0, \frac{\partial \mu}{\partial n} = \frac{\partial C}{\partial n} = 0. \tag{17}$$

Here $\partial/(\partial n)$ stands for the normal derivative; which is the derivative with respect to y for a horizontal wall, and with respect to x for a vertical wall.

3. Numerical method

3.1. Projection method

The governing equations (4)-(8) are solved numerically using the formulation of primitive variables, pressure-velocity, and using the fractional-step (or projection) method that is implemented on the basis of the finite-difference approach using the second-order formulae for spatial derivatives and the first-order formulae for time derivatives (see e.g. Ferziger and Peric, 2002; Guermond, Minev and Shen, 2006).

Namely, in the equation for the momentum balance (4), the time derivative is replaced by the formula,

$$\frac{\partial \boldsymbol{u}}{\partial t} = \frac{\boldsymbol{u}^{(n+1)} - \boldsymbol{u}^{(n)}}{\tau_0}, \tag{18}$$

where τ_0 is the time step of the marching scheme, and two superscripts, $(n+1)$ and (n), designate the 'new' and 'old' velocities that are taken at the $(n+1)$-th and (n)-th time levels, respectively.

Next, we introduce the quasi-velocity, $\widehat{\boldsymbol{u}}$,

$$\boldsymbol{u}^{(n+1)} = \widehat{\boldsymbol{u}} - \tau_0 \nabla \Pi, \tag{19}$$

that absorbs the modified pressure in equation (4),

$$\widehat{\boldsymbol{u}} = \left[\boldsymbol{u} + \tau_0 \left(-(\boldsymbol{u}\cdot\nabla)\,\boldsymbol{u} + \frac{1}{Re}\nabla^2\boldsymbol{u} - \frac{1}{M}C\nabla\mu \right)\right]^{(n)}, \tag{20}$$

The first step of the projection method is to calculate the quasi-velocity, as well as the concentration at the 'new' time level.

Substitution of the quasi-velocity (19) into the continuity equation (6) produces the Poisson equation that is used to determine the modified pressure field,

$$0 = \nabla^2\Pi - \frac{1}{\tau_0}\nabla\cdot\widehat{\boldsymbol{u}}. \tag{21}$$

Solution of the Poisson equation is the second step of the projection method. The real pressure, p, is determined using equation (7). Finally, the last, third, step of the method is to calculate the true velocity at the 'new' time level, $\boldsymbol{u}^{(n+1)}$ using equation (19).

We also adopt the velocity boundary conditions, that are set in section 2.3, for the projection method. In particular, at a rigid wall, with the use of equations (4) and (19) one can re-write the conditions for the normal and tangential components of the velocity as follows,

$$u_n^{(n+1)} = \widehat{u}_n - \tau_0\frac{\partial\Pi}{\partial n} = \tau_0\left(\frac{1}{Re}\nabla^2 u_n^{(n)} - \frac{\partial\Pi}{\partial n}\right) = 0; \quad u_\tau^{(n+1)} = 0. \tag{22}$$

At the first step of the projection method, the quasi-velocity is calculated only at inner points of the fluid domain. The condition on the normal component of the velocity is applied at the second step of the projection method, for the solution of the Poisson equation (21). For that, this condition is re-written in the form,

$$\frac{\partial\Pi}{\partial n} = \frac{1}{Re}\nabla^2 u_n^{(n)}. \tag{23}$$

The use of this condition ensures that the normal component of the velocity remains zero at a wall. The condition on the tangential component of the velocity is applied at the third step of the projection method.

3.2. Algorithm. GPU implementation

The calculations of the current work are only made possible by employing the idea of parallel computations with the use of the modern graphical processor units (GPU). In contrast to a traditional central processor unit (CPU), that may include just a few cores, a GPU includes thousands of computing cores. Each GPU core is less powerful than a CPU core, but the collective use of many GPU cores for massively-parallel computations can bring substantial advantages (Jespersen, 2010).

The advantages of the GPUs are obvious when one needs to compute several tasks simultaneously and independently (SIMD paradigm). The original use of GPUs, i.e. independent processing of thousands of pixels, is an example of the task that exactly satisfies the requirements of the SIMD paradigm. The similar requirements define a large number of other applications, for example the N-body gravity problem, the molecular dynamics simulations, or the numerical simulations with the use of the smooth particle hydrodynamics or lattice Boltzmann methods, etc. The numerical solution of partial differential equations could be also parallelized, although the particular approach for parallelization would strongly depend on the technique chosen for discretisation and solution of the equations. We use the finite difference explicit scheme which is easy for parallel implementation, where the computational domain consists of numerous nodes and each node can be processed independently on the same time step. CUDA C language is used for writing the numerical code (Sanders and Kandrot, 2010).

One of the novelties of our work is the adaptation of the projection method for implementation on GPUs. For this end, the calculations for one time step are split into several portions, so that one portion includes a parallel computation of the flow fields for a large number of the physical points using all available GPU's cores (each core computes the flow fields for one node of the computational grid).

The calculations at every time step are accomplished in three sub-steps. At the first sub-step, CPU that runs the main cycle launches three CUDA kernels (or CUDA functions) to calculate the fields of quasi-velocity, chemical potential and 'new' concentration.

At the second sub-step the Poisson equation is solved by the Jacobi method. For the Jacobi method, the elliptic Poisson equation (21) is transformed into the parabolic equation by introduction of the fictitious time, t_*,

$$\frac{\partial \Pi}{\partial t_*} = \nabla^2 \Pi - \frac{1}{\tau_0} \nabla \cdot \widehat{\boldsymbol{u}}. \tag{24}$$

To assess the convergence of the Jacobi method, an intolerance is calculated by invoking the reduction summation on GPU. There are several reduction algorithms (Harris, 2019). We use the algorithm that is based on 'Kernel 4: first add during global load', although we also performed trial calculations with the use of the different (slower) algorithms and found that the choice of reduction procedure does not impose a strong influence on the running time of the full program. A strong limitation of the reduction algorithm is the ability to sum up to 1024 elements at one time. If the total number of grid nodes exceeds 1024, then the reduction needs to be repeated. The result of the reduction (a single double-precision variable) is sent to CPU that determines whether the required accuracy is achieved.

At the third sub-step, we calculate the true velocity, and reassign the 'new' values of the pressure, velocity and concentration arrays to the 'old' ones.

We should note that a similar realization of the projection method is described in the paper by Thibault and Senocak (2009), where however the convergence of the Jacobi algorithm is not properly checked, and the calculations are simply run for a given number of iterations.

Let us also outline the arrangement of the flow fields in the computer memory, which is an important issue for the phase-field calculations, which require very high numerical resolution. Two different approaches may be suggested. The trivial approach is to consider a global domain, introducing the dummy nodes within the solid parts of the matrix. Such an approach seems to be straightforward for programming. This approach however would result in a highly inefficient use of the computer memory, and could be realised only for relatively small matrices. Another approach is the use of the indirect indexing, when all arrays are transformed into $1D$ arrays by introducing the global index, $q = q_x + (n_x + 1)q_y$, where q_x and q_y are the indexes along the x and y directions, and $(n_x + 1)$ is the number of the nodes along the x-axis. In this case, the global GPU memory is only used for the storage of the nodes within the void volume of the matrix. For efficient organisation of the computations with the use of the second approach we also create several auxiliary integer arrays that store the indexes of the neighbouring points for each node, and an array for classification of the nodes of the grid into several types, the 'inner nodes', 'left boundary', 'right boundary', 'inlet'... These auxiliary arrays are required for easy development of an universal subroutine that calculates the flow field at any physical point within the void space of the matrix. The current numerical algorithm operates 9 double precision arrays for the flow fields: 4 arrays for the fields of velocities (two components of the true and quasi-velocity), 2 for the pressure field (the pressure field at two time levels), 2 for the concentration field (again, for two time levels) and 1 for the chemical potential. The addition of the above-defined integer auxiliary arrays increases the memory usage by $\approx 25\%$, which is much more efficient use of the memory as compared with the first approach when the nodes within the solid matrix are engaged into computations.

It should be also clarified that a GPU operates as a co-processor for a CPU: the computer program is launched at a CPU that controls implementation of the program, sending the data and instructions to a GPU. A CPU has its own operative memory, however, the data exchange between the CPU's RAM and the GPU's global memory is characterised by a greater latency. For calculations, all arrays that represent the different flow fields are located in the GPU's global memory; the auxiliary arrays are stored in the CPU and GPU memory; all constants that define the problem are stored in the fast constant GPU memory.

All flow fields are periodically copied back into a CPU (after a large number of the time steps) for calculation of the integral characteristics and for saving of the flow fields for further visualisations.

It is difficult to measure the performance advantages of an implemented parallel algorithm due to essential differences between GPU and CPU computers. We can however note that the running time of the parallel code on an NVidia Tesla V100 computer is almost hundred times less as compared with with the running time of the serial code on an i7 computer.

4. Results

4.1. Single-phase flow

To obtain the reference values and to verify the numerical approach, we first solve the simplified equations modelling the flow of a single-phase fluid through a single capillary and through a matrix of capillaries. In this model the

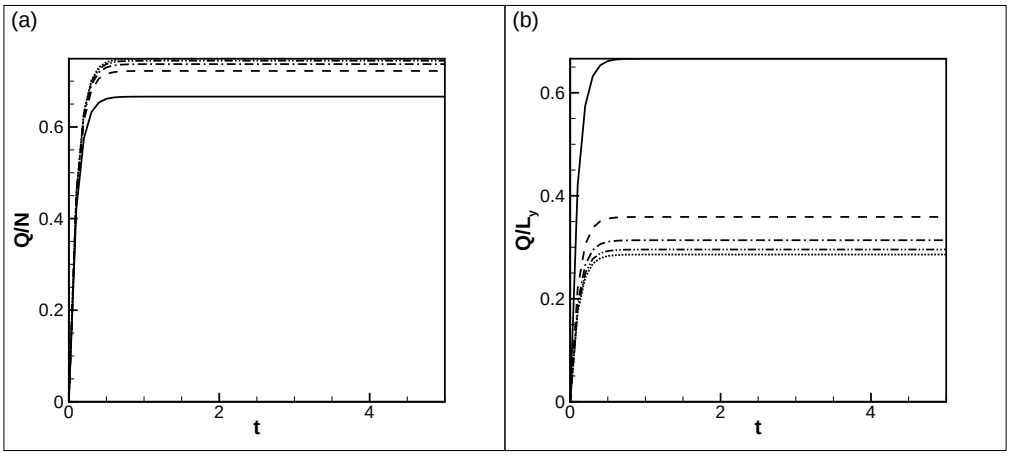

Figure 2: The volumetric flow rate divided by the number of the horizontal capillaries (a) and by the width of the outlet side of a matrix. The results are shown for a single capillary (solid line) and for matrices with 2×2 (dashed line), 3×3 (dash-dotted line), 4×4 (dash-dot-dotted line), and 5×5 (dotted line) elements. The results are obtained for a single-phase flow ($Re = 1$ and $Pe_0 = 10^4$).

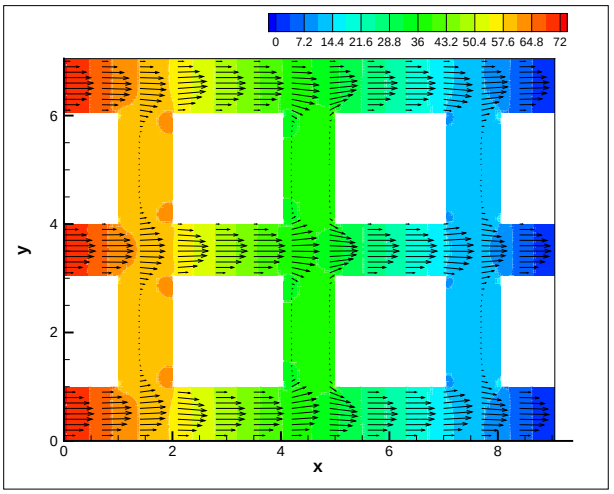

Figure 3: The fields of pressure (isolines) and velocity (vectors) for a single-phase flow through the matrix of 3×3 elements. The results are obtained for a single-phase flow ($Re = 1$ and $Pe_0 = 10^4$).

liquids are distinguished using the concentration field, although the capillary effects are completely neglected, and the diffusion is modelled using the classical Fick's law. This approach is traditionally used to describe the evolution of two miscible liquids. The governing equations that define the model include the equations for the momentum, species and mass balances:

$$\frac{\partial \boldsymbol{u}}{\partial t} + (\boldsymbol{u} \cdot \nabla)\, \boldsymbol{u} = -\nabla p + \frac{1}{Re} \nabla^2 \boldsymbol{u}, \tag{25}$$

$$\frac{\partial C}{\partial t} + (\boldsymbol{u} \cdot \nabla)\, C = \frac{1}{Pe_0} \nabla^2 C, \tag{26}$$

$$\nabla \cdot \boldsymbol{u} = 0. \tag{27}$$

matrix	1×1	2×2	3×3	4×4	5×5	6×6
Q_1/L_y	2/3	0.359	0.314	0.296	0.286	0.280
k	0.0834	0.0449	0.0393	0.0370	0.0358	0.0350

Table 1
The volumetric flow rates of the single-phase flow through the matrices with different number of the elements, and the base permeabilities of the matrices.

These equations are written in the non-dimensional form that is obtained using the same scales as used to non-dimensionalise the phase-field equations (namely, for the scales of the length, velocity, time and pressure, we use h, V_*, h/V_* and $\rho_* V_*^2$, respectively). The definition of the Reynolds number coincides with the one written above, but the definition of the Peclet number is based on the classical diffusion coefficient (that is missing in the phase-field theory),

$$Re = \frac{\rho_* V_* h}{\eta_*},\ Pe_0 = \frac{\rho_* V_* h}{D_*}. \tag{28}$$

Equations (25)-(27) are solved numerically using the projection method explained in the section 3.1, with the difference that the modified pressure simply equals pressure p.

The numerical results obtained with the use of the traditional approach are depicted in figures 2 and 3. One sees that after a short initial adjustment period, the flow rate through the matrix becomes constant. In a single capillary, the flow rate for the established (steady) flow equals to $Q_0 = 2/3$, which corresponds to the Poisseuille flow profile. In a matrix, the fluid flows only through the horizontal capillaries, and the fluid stays stationary in the vertical elements. The flow rate through the matrix can be averaged by the number of the horizontal capillaries, and this quantity is shown in figure 2a. One sees that the addition of the new elements to the matrix makes the flow rate slightly greater than $2/3$, which is explained by acceleration of the fluids within pores, where there are no no-slip boundaries. The results quickly converge, and the flow rates determined for matrices with 4×4 and 5×5 elements are already virtually equal. The other option is to report the total flow rate divided by the width of the outlet boundary, and this quantity is plotted in figure 2b. Addition of the new element to the matrix reduces the total flow rate, although, a fast convergence of the results upon the increase of the size of the matrix is also observed.

Figure 3 depicts the structure of an established flow field for a matrix with 3×3 elements. One sees that the pressure linearly drops along the matrix, and the flow has a parabolic profile in horizontal capillaries, although the profile is wider within the pores.

The calculations of the flow rate for a single-phase flow can be used for determination of the base permeability of a matrix.[2] Namely, in the non-dimensional form, the Darcy law reads,

$$\boldsymbol{q} = -k Re \nabla p. \tag{29}$$

Here the vector $\boldsymbol{q}$ stands for the volumetric flow rate per unit surface (scaled by V_*) and k is the non-dimensional permeability (scaled by h^2).

For a considered problem, the total volumetric flow rate through a porous matrix is given by the following expression,

$$Q_1 = L_y k Re \frac{\Delta p}{L_x} = 8 k L_y. \tag{30}$$

Thus, the permeability of a matrix is given by $Q_1/(8L_y)$. Using the results shown in figure 4b, one may obtain the permeabilities of different matrices, which are summarised in Table 1. When, the number of the elements in the matrix grows, the permeability converges to the value of $k \approx 0.035$. The dimensional value of the permeability is $\sim 0.035 h^2 \sim 10^{-10} m^2$ (for $h \sim 10^{-4} m$).

In this work we are interested in the flow of two liquids, and thus we formally may also use the extended Darcy theory for multiphase flows. For the traditional model, however, the capillary pressure is always equal to 0, and the relative permeabilities are equal to 1 for both phases.

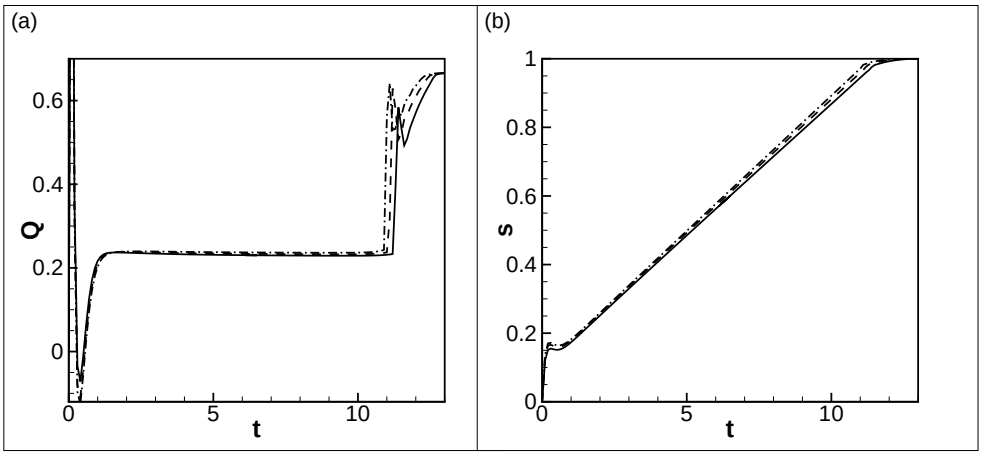

Figure 4: The volumetric flow rate (a) and the saturation of an injected liquid (b) for the liquid/liquid displacement flow in a single capillary tube. The data are obtained for $Cn = 10^{-4}$, $M = 2.5 \cdot 10^{-4}$, $Re = 1$, and $Pe = 10^4$, for four different resolutions, with the spatial step: 1/400 (dash-dotted line), 1/500 (dashed line) and 1/600 (solid line).

4.2. Two-phase flow. A single capillary

First, we would like to show the results that are obtained for the liquid/liquid displacement flow in a single capillary. Figure 4 depicts the temporal changes of the flow rate, $Q = \int_0^1 u_x dy$, through the capillary (owing to incompressibility of the fluids, the flow rate has the same values at every cross section of the capillary), and the saturation of the displacing liquid in the capillary, $s = 1/2 - < C >$ (here $< C >= \int_V C dV$ is the average concentration of the liquid/liquid mixture in the capillary).

The data shown in figure 4 are obtained for the uniform numerical grids that include the different numbers of the computational nodes, with the spatial resolutions of 1/400, 1/500 and 1/600. One sees that the results obtained for the numerical grids of the different finesse are very close, thus even the mesh with the spatial step of 1/400 would be sufficient to produce the accurate results. The constraints on the resolution are primarily determined by (i) the capillary effects, controlled by the surface tension coefficient σ, by (ii) the tube length and the Reynolds number that define the magnitude of the imposed pressure gradient, and by (iii) the Peclet number that determines the strength of the diffusion effects that is an additional mechanism of dissipation. Below, all results for the flow through a single capillary are shown for the numerical grid with the resolution of 1/600; and the results for the flows in matrices are obtained with the numerical resolution of 1/400 (for an additional check of the numerical convergence, the results for a matrix with 4×4 elements are also re-obtained with the resolution of 1/600).

In figure 4 one can also observe that the displacement flow starts from a complex adjustment period. Initially, the pressure gradient over-stretches the liquid/liquid meniscus, and this is followed by the contraction of the meniscus that even pushes the fluids in the reverse direction, opposite to the externally imposed pressure gradient, and which is defined by the negative values of the flow rate. The initial flow adjustments last for about 1 unit of non-dimensional time (~ 0.01s). The magnitude and duration of the contraction strongly depend on the surface tension effects. Later, the shape of the meniscus is stabilised and the flow rate is set to a constant value. When the meniscus reaches the outlet end of the capillary, the flow rate suddenly increases, ultimately saturating at the value of $Q \sim 0.667$, which corresponds to the Poisseuille solution for the single-phase flow in the capillary.

The changes in the values of the flow rate can be easily correlated with the transformations of the liquid/liquid meniscus as seen in figure 5, where the fields of concentration, pressure and velocity are shown for the different time moments. At the first instances after switching on the pressure difference, the meniscus' shape rapidly evolves, from a flat shape that is set by the initial condition to a curved interface which shape is enforced by the imposed pressure gradient (see figure 5a-d). Later, the piston-like displacement of the liquid from the capillary is observed (see figure 5e-f). The speed of the meniscus' propagation is controlled by several parameters, including the capillary pressure, that is determined by the interface shape: when the shape of the meniscus is stabilised, the capillary pressure and the flow

[2]The permeability of a matrix is frequently anisotropic, and this is also the case for the considered matrix; hence, we obtain only the value of permeability for the flow along the x-direction of a matrix.

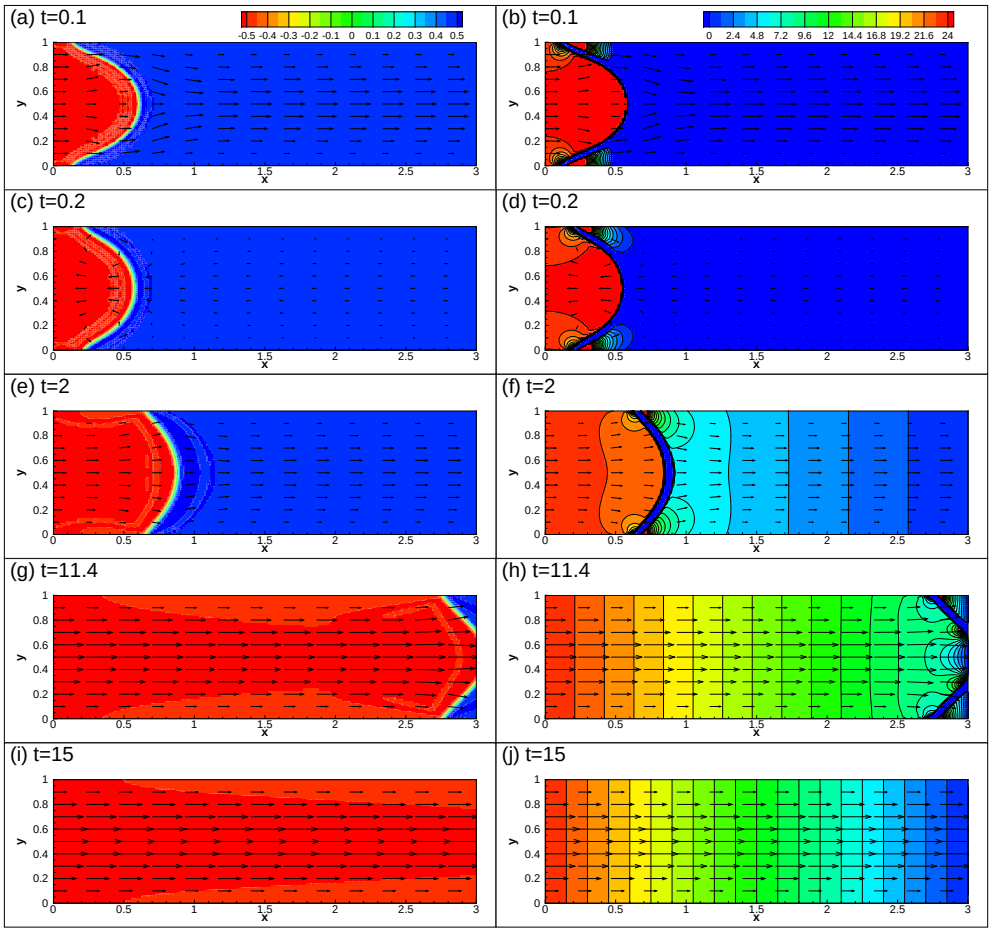

Figure 5: The fields of concentration (left column) and pressure (right column) in a single capillary at three different time moments. The arrows designate the field of velocity. The data are obtained for $Cn = 10^{-4}$, $M = 2.5 \cdot 10^{-4}$, $Re = 1$, and $Pe = 10^4$.

rate become constant. When the meniscus' tip reaches the right end of the capillary (figure 5g-h), the magnitude of the capillary pressure rapidly drops, which also results in the jump of the value of the flow flux. The displaced liquid however still remains attached to the walls of the capillary. Gradually, the liquid at the tube walls gets completely washed out from the capillary, so finally the single phase flow is observed (figure 5i-j).

Figure 6 depicts the profiles of the concentration and the chemical potential along the capillary and at the wall. To demonstrate the mesh independence of the results, the profiles are shown for the meshes with the $1/400$ and $1/600$ step sizes. One sees that the interface remains sharp. For lower values of the surface tension coefficient, that is defined by equation (12), the shape of the meniscus changes while the meniscus moves along the capillary (the interface stretches), although for sufficiently high values of the surface tension coefficient the shape of the meniscus remains unaltered during its motion in the capillary, so the displacement occurs in a piston-like manner (Prokopev et al., 2019). The levels of the concentration within the neighbouring phases remain constant, equal to $\pm 1/2$. At the sides of the interface there are some tiny overshootings in the levels of concentration (with the levels of concentration lying outside the physically-relevant range, $-1/2..1/2$), although, an increase in the numerical resolution makes the amplitude of the overshootings smaller.

In the phase-field simulations the gradients of the chemical potential define the rate of diffusive mass transfer through the interface. One sees that the chemical potential has a nearly constant (zero) value everywhere, except for a narrow zone near the interface. We are interested in an immiscible liquid/liquid displacement, and conduct all simulations for sufficiently high values of the Peclet number. In this case the diffusive mass transport is negligibly small as compared to the convective transport, except for the vicinity of the wall. Owing to the no-slip boundary

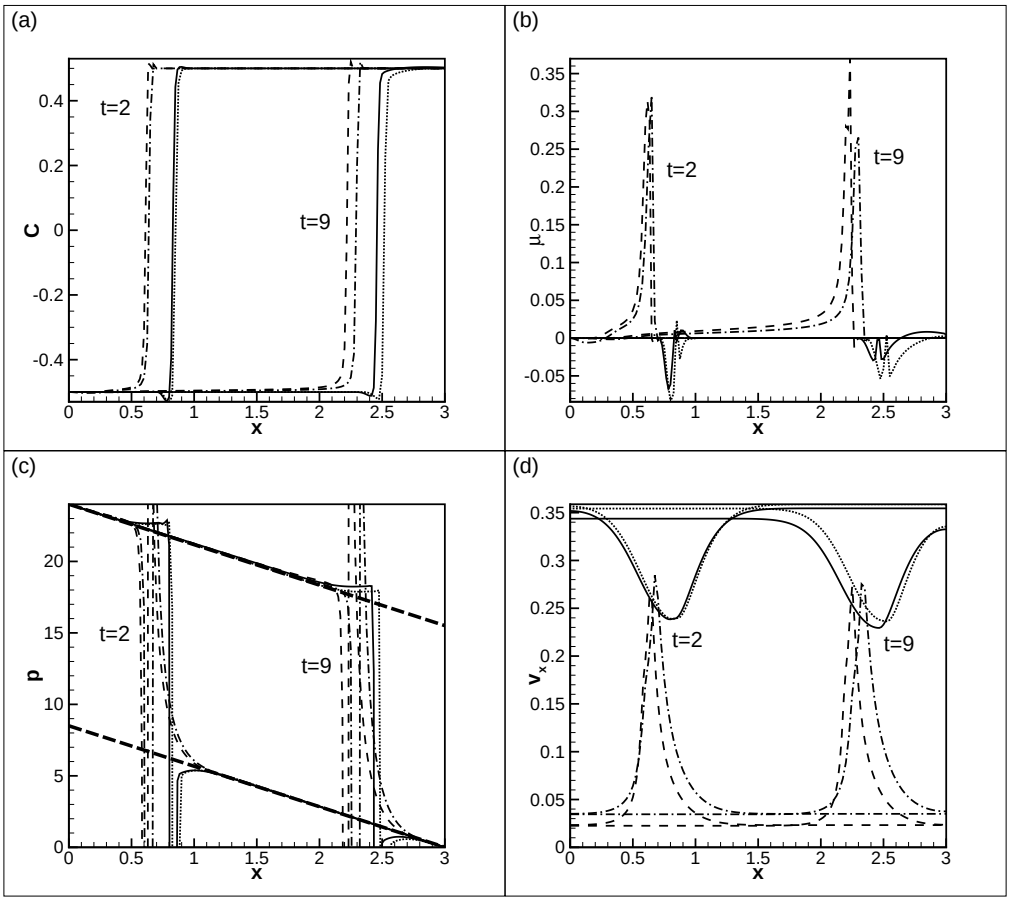

Figure 6: The profiles of the fields of concentration, chemical potential, pressure, and x-component of the velocity along the centreline (solid and dotted lines) and along the wall (dashed and dash-dotted lines; the x-component of the velocity is 0 at the wall, and thus the velocity profiles are shown near the wall, 10 grid nodes from the wall). The results are shown for $M = 2.5 \cdot 10^{-4}$, $Cn = 10^{-4}$, $Re = 1$, $Pe = 10^4$, for two numerical grids with the step size of $1/400$ (dotted and dash-dotted lines) and $1/600$ (solid and dashed lines). In (c), two thick long-dashed lines are defined by equations $p = 24 - 2.83x$ and $p = 8.5 - 2.83x$.

condition the flow velocity is zero at the wall, although as one can see in figures 4 and 6, the contact line moves. The motion of the contact line in the phase-field model was earlier examined by Jacqmin (2000). To explain movements of the contact line other numerical approaches, e.g. the volume-of-fluid or level-set methods, require incorporation of an additional parameter, the slip length, into the no-slip boundary condition. The phase-field approach however is capable of explaining the motion of the contact line on the basis of the solution of the governing equations using the standard no-slip boundary condition: the shape and motion of the contact line is derived from the structure of the concentration field, similarly to the shape and motion of the meniscus in the bulk. Jacqmin (2000) concludes that movements of the contact line are controlled by the Peclet number (instead of the slip length).

Figure 6c depicts the horizontal profiles of the pressure field. The displacement flow is driven by the difference in the pressure levels at the capillary's ends, which are $p_1 = 8L_x/Re = 24$ at the inlet (left end) and $p_2 = 0$ at the outlet (right end). While the liquid/liquid meniscus remains within the capillary, the pressure profile consists of two straight lines with the equal negative slopes and a jump that is located at the place of the interface. The height of the jump defines the value of the capillary pressure. The pressure profiles generally agree with the common expectation that the pressure decreases linearly along the tube with a jump transition across the interface. The smaller deviation of the pressure profile from the linear trend may be only observed near the meniscus. The deviation from the linear profile can be also observed when the meniscus reaches the outlet end of the capillary, which should be explained by some imperfection of the approximations accepted for our simulations. In particular, the vertical velocity is assumed

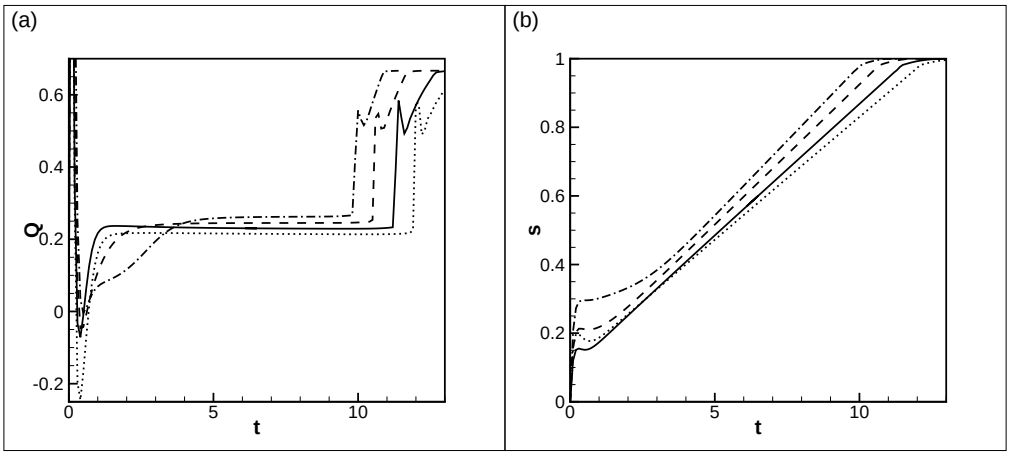

Figure 7: The volumetric flow rate (a) and the saturation of an injected fluid (b) for the liquid/liquid displacement in a single capillary tube. The data are obtained for $Cn = 10^{-4}$, $M = 2.5 \cdot 10^{-4}$, $Re = 1$, and for different Peclet numbers $Pe = 2.5 \cdot 10^3$ (dash-dotted line), $Pe = 5 \cdot 10^3$ (dashed line), $Pe = 10^4$ (solid line) and $Pe = 2 \cdot 10^4$ (dotted line).

to be zero at the outlet, but the vertical velocity is not zero near the meniscus. In addition, the pressure at the outlet is set to be zero. The pressure at the inner side of the meniscus is greater than at the outer side, and when the meniscus just touches the outlet the pressure experiences an abrupt change, that can be noticed by a faster than linear drop in the pressure near the outlet end. This difference from the linear trend near the outlet end can be observed until the displaced fluid is fully removed from the capillary.

The major difference from the classically expected distribution of the pressure is however observed in the interfacial zone, where the computed pressure profile exhibits a peak with the large negative values. For the sake of clarity of the pictures, the pressure levels in figure 6c are cut by 0 and 24, which are the pressure levels at the capillary's ends. The similar pressure profiles were already observed in our earlier study (Prokopev et al., 2019), where we concluded that such a pressure distribution is an artefact of the phase-field model, that is determined by the choice of the free energy function. The pressure cannot be measured within the transition zones, and thus the peculiar pressure profiles in the transition zone may not be validated. For the practical use of our numerical results, it is much more important that the pressure distributions outside the interfacial zones agree with the classical expectations, and that the predicted values of the capillary pressure are correct. In the vicinity of the contact line, the pressure profiles are also quite complex, with the very high positive pressure peaks located outside of the interfacial zones, which should be associated with the overall mass balance near the wall.

Figure 6d depicts the profile of the x-component of the velocity along the capillary. The velocity profile become complex near the meniscus, with the maximum values of velocity located near the walls. The vortex motion is formed near the meniscus that slows down the motion in the middle part of the capillary and accelerates the motion near the capillary's walls.

The role of the Peclet number on the dynamics of the liquid/liquid displacement is illustrated in figures 7 and 8. An increase of the value of the Peclet number leads to convergence of the numerical results to some limiting curves. The effect of the change of the Peclet number is primarily seen during the initial adjustment of the meniscus. The amplitude of the meniscus' contraction becomes stronger at higher Peclet numbers. The contraction of the meniscus is determined by the motion of the contact lines. At lower Peclet numbers (stronger diffusion) the sliding of the contact lines along the walls (which is explained by diffusion) occurs easier, which reduces the over-stretching of the liquid/liquid meniscus and reduces the amplitude and the effect of the meniscus' contraction on the overall flow. At the later time moments, at sufficiently high values of the Peclet numbers, the shape and motion of the meniscus are only slightly dependent on the value of the Peclet number. At higher Peclet numbers the flow becomes slightly slower, which is also explained by slower movement of the contact line.

We are interested in the dynamics of an immiscible sharp interface. Although, for the sake of numerical treatment, the interfacial boundary is smeared. To generate the physically relevant results, it is necessary to obtain the results in the limit of a sharp interface, which can be obtained by tending the Cahn and Mach numbers to zero keeping their

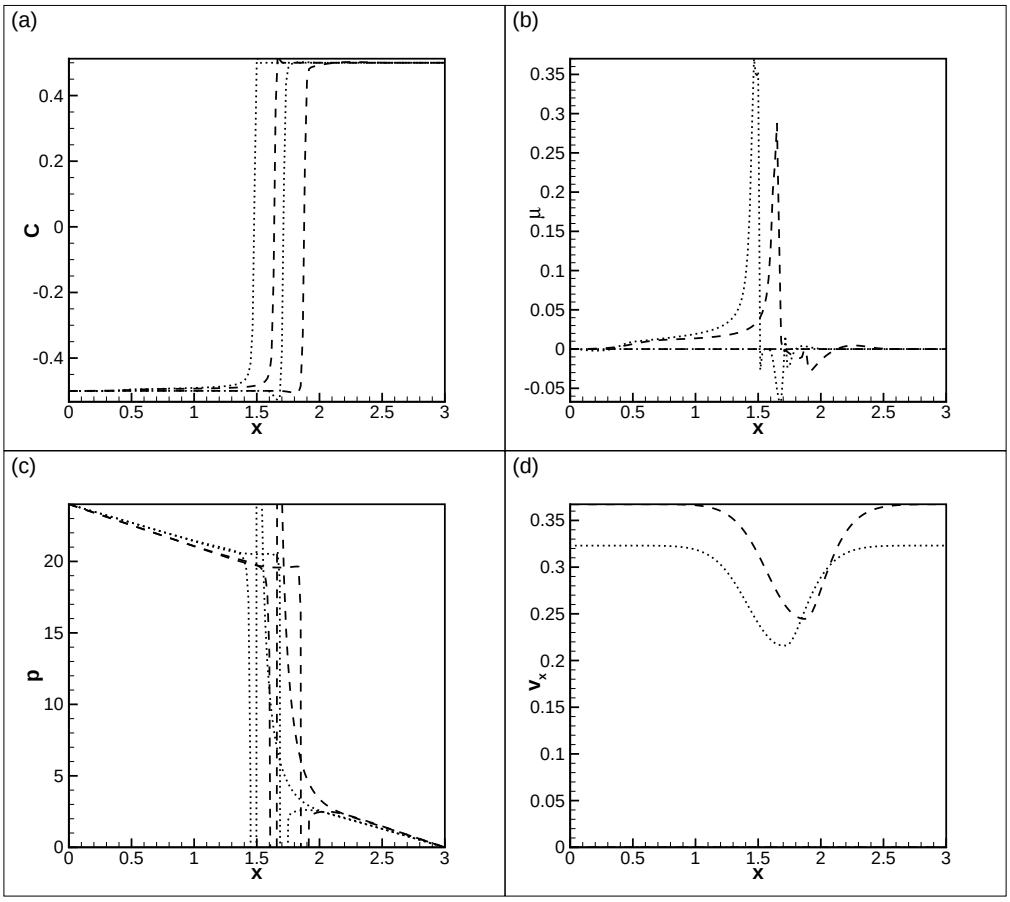

Figure 8: The profiles of the fields of concentration, chemical potential, pressure, and x-component of the velocity along the centreline and along the wall at $t = 6$. The results are shown for $M = 2.5 \cdot 10^{-4}$, $Cn = 10^{-4}$, $Re = 1$ for two Peclet numbers $Pe = 5 \cdot 10^3$ (dashed line) and $Pe = 2 \cdot 10^4$ (dotted line).

ratio, $\gamma = \sqrt{Cn}/M$, constant. Figure 9 depicts the results of the similar analysis (for $\gamma = 40$). One sees that the major difference between the curves occurs at the initial moments. The effect of the meniscus' contraction on the overall flow becomes weaker at lower Cahn numbers (for thinner interfaces). The convergence of the numerical results upon the gradual decrease of the Cahn and Mach numbers can be also seen, indicating that for the given γ, the behaviour of the studied system may be accurately described by taking $Cn = 10^{-4}$ and $M = 2.5 \cdot 10^{-4}$.

The parameter γ is proportional to the surface tension coefficient. The estimations given in section 2.2 indicate that in order to reproduce the behaviour of a real interface, one needs to consider quite large values of this parameter, $\gamma \sim \sigma \sim 10^3$, which is beyond the reach of our computational capabilities (strengthening the surface tension effect requires the use of finer temporal resolution for correct description of the initial adjustments of the meniscus shape). However, the simulations performed for different values of the parameter γ reveal the convergence of the numerical results upon the gradual increase of γ. This in particular can be seen in figure 10 where the results are shown for $\gamma = 20$, 40, 60 and 80. In order to model the displacement flow at strong capillary effects (typical for immiscible interfaces), it is sufficient to take $\gamma \geq 40$. The differences in the results obtained with higher surface tension forces would be only observed at the initial very short adjustment period, when the meniscus adjusts to its steady shape (and this shape remains unchanged during the entire displacement run).

In this work we also aim to correlate the results of the pore-level analysis with the macroscopic description of the multiphase flows in the porous medium. In particular, our results can be used to determine the capillary pressure (if a capillary is used to represent a typical element of the porous matrix).

For a two-phase displacement flow in a capillary, the flow rate is determined by the Washburn equation (Washburn,

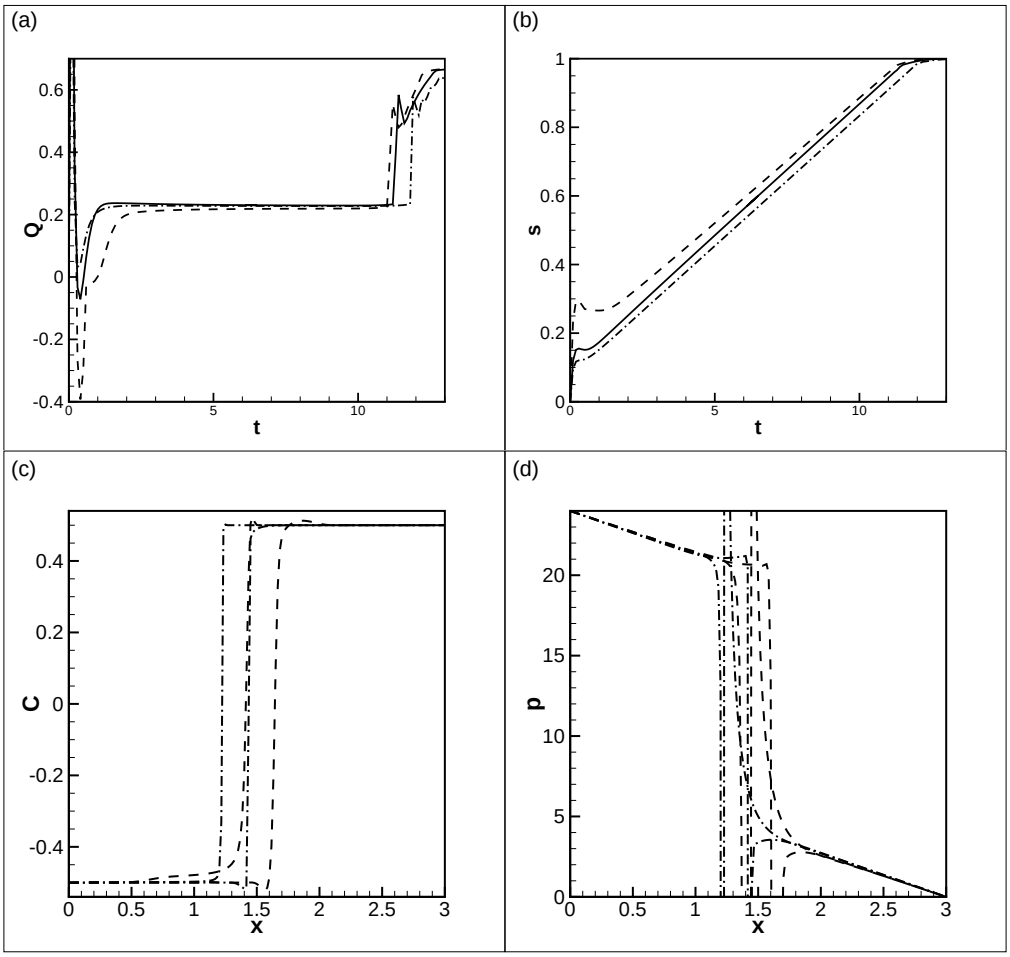

Figure 9: (a,b) The volumetric flow rate (a) and the saturation of an injected fluid (b) for the liquid/liquid displacement in a single capillary tube. (c,d) The profiles of the fields of concentration (c) and pressure (d) along the centreline and along the wall at $t = 5$. The data are obtained for $Re = 1$, $Pe = 10^4$ and $Cn = 4 \cdot 10^{-4}$, $M = 5 \cdot 10^{-4}$ (dashed lines), $Cn = 10^{-4}$, $M = 2.5 \cdot 10^{-4}$ (solid lines) and $Cn = 2.5 \cdot 10^{-5}$, $M = 1.25 \cdot 10^{-4}$ (dash-dotted lines).

1921),

$$Q_2 = \frac{Re}{12L_x}(p_1 - p_2 - p_c) = \frac{2}{3} - \frac{Re}{12L_x}p_c. \tag{31}$$

Here p_c is the capillary pressure. Equation (31) can be rewritten to provide a quick evaluation of the capillary pressure, namely

$$p_c = \left(1 - \frac{Q_2}{Q_1}\right)(p_1 - p_2). \tag{32}$$

For our base numerical run shown in figures 4-6, the so-calculated capillary pressure is $p_c = 15.5$ (the pressure difference between the ends of the tube is $(p_1 - p_2)$=24), which is confirmed by the pressure curves shown in figure 6. Indeed, one can see that the pressure slopes are the same in both liquids, and the pressure drops across the meniscus by the value of 15.5. This value of the capillary pressure remains independent of saturation until $t \sim 13$ when the capillary becomes fully saturated by the displacing fluid ($s = 1$) and hence the flow flux becomes equal to $Q_1 = 0.667$.

4.3. Two-phase flow. 2×2 matrix

The numerical results for a matrix built of several capillaries turn out to be quite similar to the observations reported above for the displacement flow in a single capillary. In particular, the snapshots of the flow fields for the matrix with

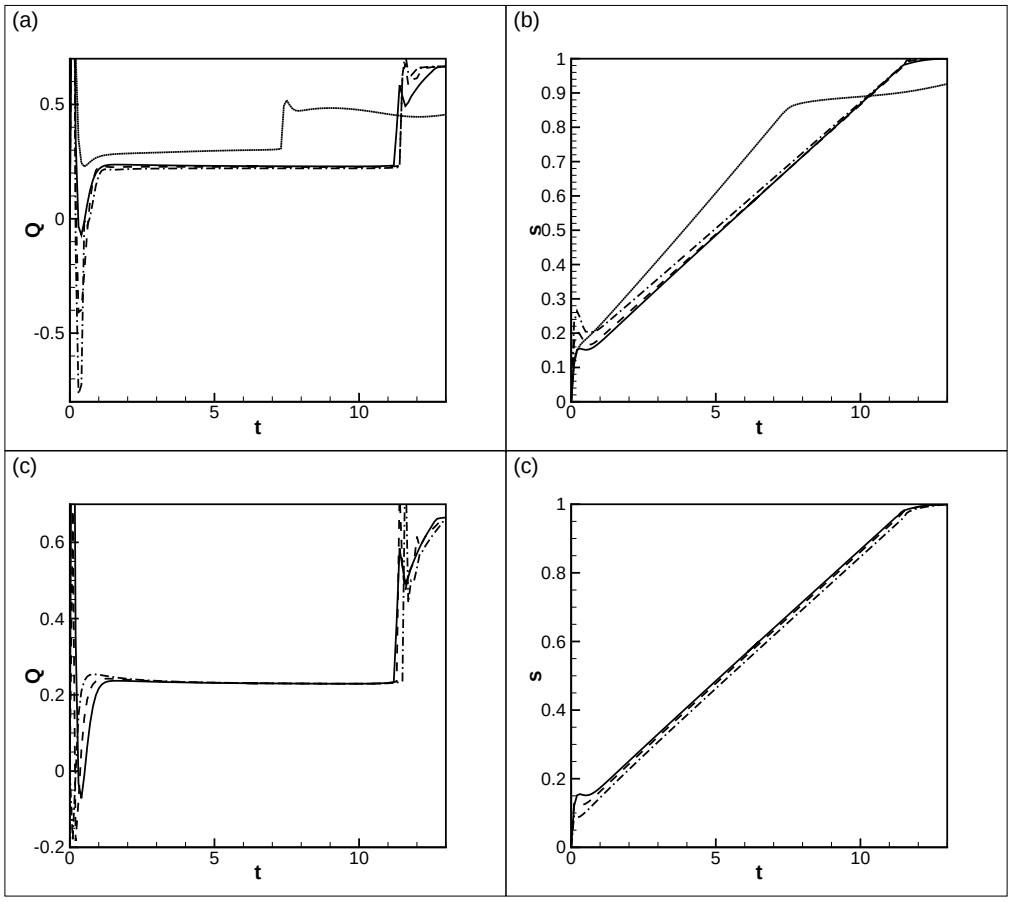

Figure 10: The volumetric flow rate (a,c) and the saturation of an injected fluid (b,d) for the liquid/liquid displacement in a single capillary tube. (a,b) The data are obtained for $Cn = 10^{-4}$, $Re = 1$, $Pe = 10^4$, and different values of the Mach number, $M = 5 \cdot 10^{-4}$(dotted lines), $M = 2.5 \cdot 10^{-4}$ (solid lines), $M = 1.66 \cdot 10^{-4}$(dashed lines) and $M = 1.25 \cdot 10^{-4}$ (dash-dotted lines). (c,d) The data are obtained for $Cn = 10^{-4}$, $Pe = 10^4$, and different values of the Mach number, $Re = 1$, $M = 2.5 \cdot 10^{-4}$ (solid lines), $Re = 0.5$, $M = 1.25 \cdot 10^{-4}$(dashed lines), and $Re = 0.25$, $M = 6.25 \cdot 10^{-5}$ (dash-dotted lines).

2×2 elements are depicted in figure 11. The changes in the flow rate and saturation with time are shown in figure 12. One may identify the same stages in the dynamics of the liquid/liquid displacement. After the initial adjustment (when the meniscus' shape experience some capillary oscillations), the flow rate becomes nearly constant, with the value lower than the rate for a single-phase flow, which is obviously explained by the dragging effect imposed by the capillary forces. There are two noticeable bumps on the level of the flow rate, which correspond to the moments when the menisci pass through the pores of the matrix. At these moments, the meniscus' shape changes, which alters the capillary pressure. When the tips of the menisci reach the right end of the matrix, the flow rate starts rising, eventually, reaching another constant level, which is already closer to (although still different from) the level of the single-phase flow. At this latter period, the displaced fluid still fills in the vertical capillaries of the matrix, from where it may not be removed by the simple pumping of the displacing fluid. The remainders of the displaced fluid in the matrix affect the motion of the second fluid, so the final flow rate is lower than the rate for the single phase flow (the dotted lines in figure 12).

Our numerical results permit an easy calculation of the capillary pressure that characterises the displacement flow through the matrix, which is demonstrated in figure 13. Surprisingly, application of formula (32) to a more complex geometry than a single capillary still generates an excellent prediction of the capillary pressure. For instance, for a matrix with 2×2 elements, the flow rate for a single-phase flow is $Q_1/L_y = 0.359$. The flow rate for a two-phase flow (until the meniscus remains within the matrix) slightly varies, for instance, $Q_2/L_y = 0.156$ at $t = 1$ and $Q_2/L_y = 0.191$

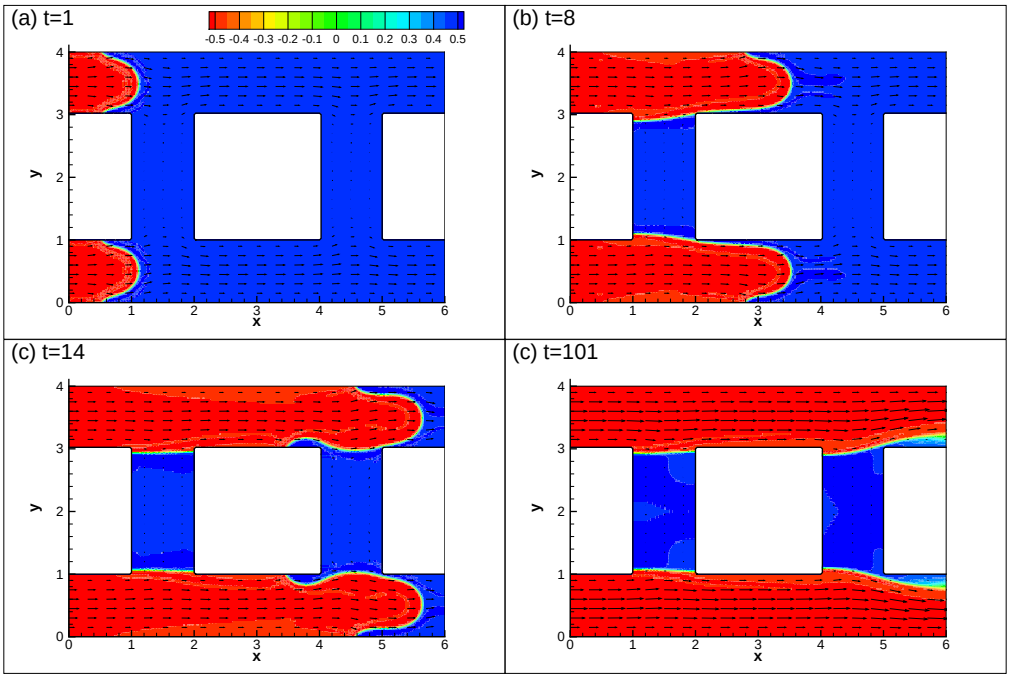

Figure 11: The snapshots of the concentration (isolines) and velocity (vectors) fields for a matrix with 2×2 elements. The arrows are scaled in accordance with the magnitude of the velocity. The data are obtained for $Cn = 10^{-4}$, $M = 2.5 \cdot 10^{-4}$, $Re = 1$, and $Pe = 10^4$. The pressure difference between the ends of the capillary is $p_1 = 8L_x/Re = 48$.

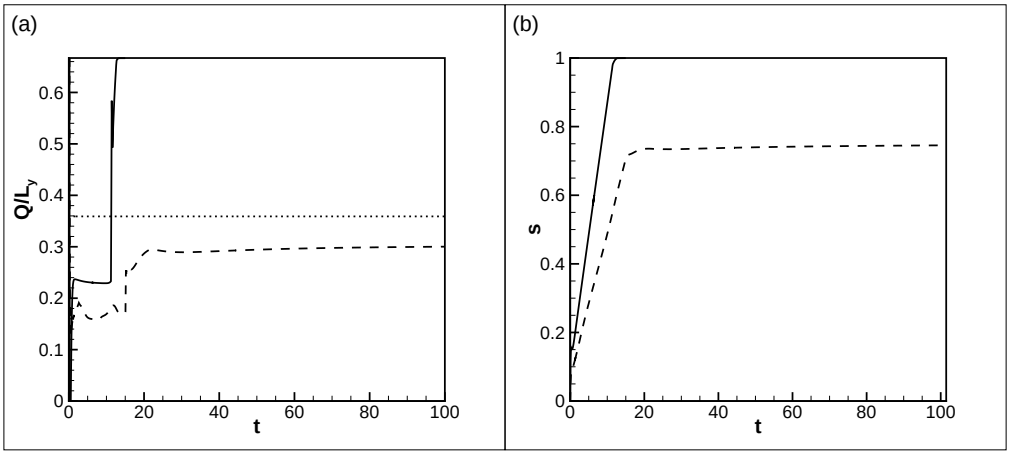

Figure 12: The volumetric flow rate (a) and the saturation of an injected fluid (b) for the liquid/liquid displacement in a single capillary (solid lines) and in a matrix with 2×2 elements (dashed lines). The data are obtained for $Cn = 10^{-4}$, $M = 2.5 \cdot 10^{-4}$, $Re = 1$ and $Pe = 10^4$. The dotted line in (a) indicates the value of the volumetric flow in a matrix with 2×2 elements for a steady single-phase flow.

at $t = 2.7$. Using formula (32) one obtains that the capillary pressure equals 27.1 and 22.5, respectively. These values are confirmed by the pressure fields shown in figure 13, where one sees that the pressure slopes in both phases (within the horizontal elements of the matrix) are equal, and the values of the slopes can be well explained by taking into account the predicted drops in pressure across the interface. In figure 13 one can also see that the pressure remains nearly constant in the vertical elements of the matrix, where the fluid is stagnant.

Interpretation of a steady process that is observed towards the end of the numerical run shown in figure 12 (when the changes in the value of the flow rate and saturation from $t \approx 64$ to $t \approx 100$ do not exceed 1%) is not obvious.

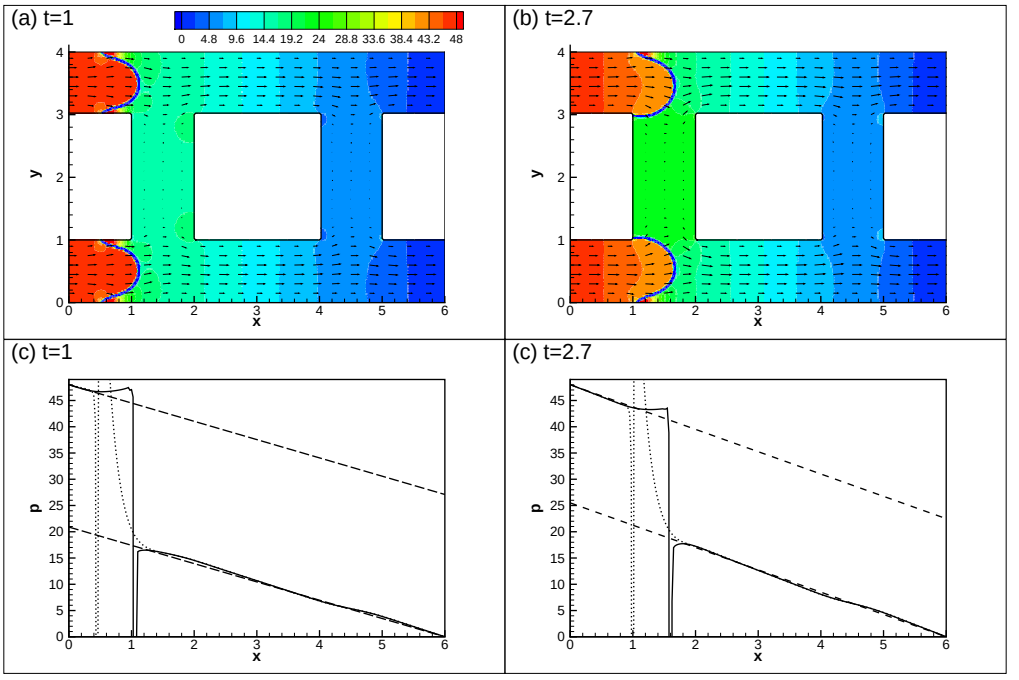

Figure 13: (a,b) The fields of pressure (isolines) and velocity (arrows) for a matrix with 2×2 elements. (c,d) The pressure profiles are shown along the bottom wall (dotted lines) and along the centreline of the lower tube (solid lines). The dashed lines depict the lines, $p_1-(p_1-p_c)x/L_x$ and $-(p_1-p_c)(x-L_x)/L_x$, with $p_c=27.1$ in (c), and $p_c=22.5$ in (d), respectively. The data are obtained for $Cn=10^{-4}$, $M=2.5\cdot10^{-4}$, $Re=1$, and $Pe=10^4$. The pressure difference between the ends of the capillary is $p_1=8L_x/Re=48$.

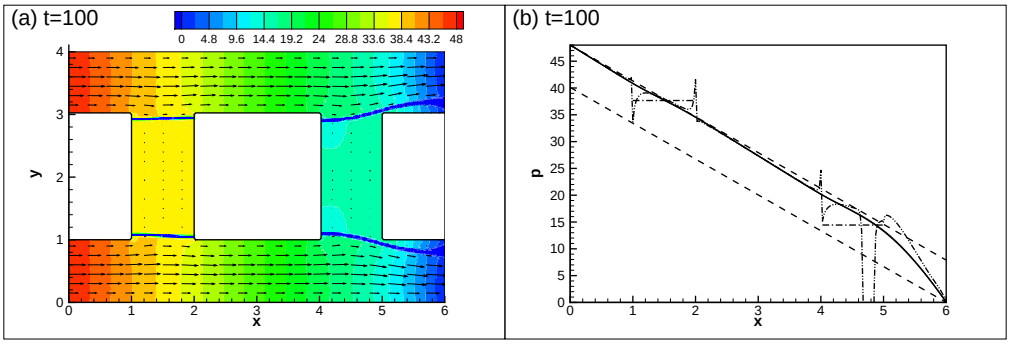

Figure 14: (a) The fields of pressure (isolines) and velocity (arrows) for a matrix with 2×2 elements. (b) The pressure profiles are shown along the bottom wall (dotted line), along the centreline of the bottom tube (solid line), along the upper boundary of the lower tube (dash-dot-dotted line), and along the middle of the matrix (dash-dotted line). The dashed lines depict the lines, $p_1-(p_1-p_c)x/L_x$ and $-(p_1-p_c)(x-L_x)/L_x$, with $p_c=7.89$. The data are obtained for $Cn=10^{-4}$, $M=2.5\cdot10^{-4}$, $Re=1$, and $Pe=10^4$. The pressure difference between the ends of the capillary is $p_1=8L_x/Re=48$ (as $L_x=6$ and $Re=1$).

It is tempting to explain the lower flow rates simply by the presence of the first fluid in the vertical elements of the matrix, which reduces the effective permeability of the matrix. The pressure profiles depicted in figure 14 however indicate that a different explanation is needed. Even in the steady-state regime, the pressure distribution along the matrix remains complex: the pressure distribution along the horizontal elements of the matrix changes following a linear law, $p_1-(p_1-p_c)x/L_x$, but with a jump by the value of $p_c=7.89$ that is observed near the outlet end of the matrix. In the case of a single capillary, at the moment when the meniscus' tip reaches the outlet end, so the displaced liquid remains only at the walls, the pressure distribution is characterised by the similar profile with a simple jump

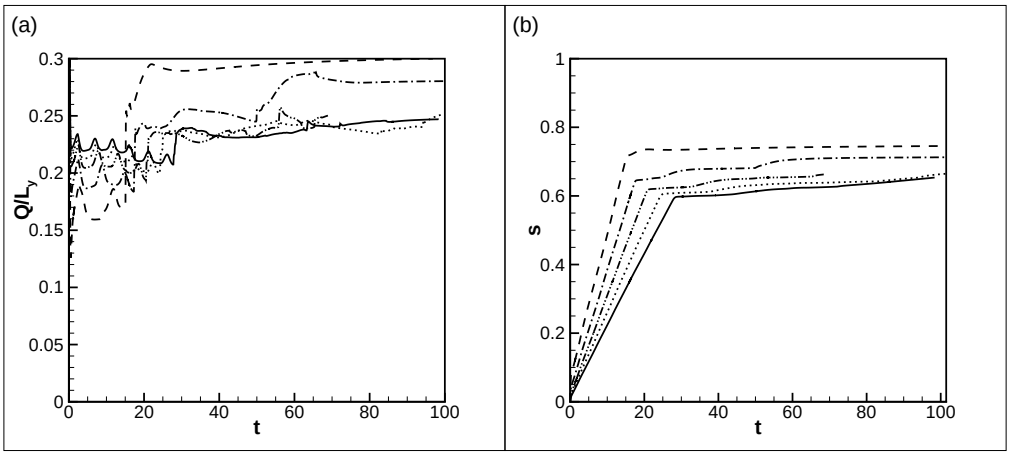

Figure 15: The volumetric flow rate (a) and the saturation of an injected fluid (b) for the liquid/liquid displacement in matrices with 2×2 (dashed lines), 3×3 (dash-dotted lines), 4×4 (dash-dot-dotted lines), 5×5 (dotted lines), and 6×6 (solid lines) elements. The data are obtained for $Cn = 10^{-4}$, $M = 2.5 \cdot 10^{-4}$, $Re = 1$ and $Pe = 10^4$.

at the outlet end. In a capillary, the similar pressure profiles are however observed during a short period, until the displaced fluid is fully removed from the tube. In the case of the matrix, the full displacement of the displaced liquid never occurs and the pressure profile along the matrix never becomes linear.

4.4. Two-phase flow. Larger matrices

Figure 15 depicts the temporal changes in the flow rates and saturations in larger matrices. One sees that the liquid/liquid displacement in all matrices follow the same stages that were outlined above: a short adjustment period with menisci oscillations, a propagation of the displacement front through the matrix (when all menisci remain within the matrix), a later stage when the tips of menisci have already reached the outlet end and the displaced liquid is scratched from the walls, and the latest steady stage when the part of matrix (the vertical elements) still remain saturated with the displaced liquid, although further pumping does alter the distribution of the liquids within the matrix. One can also see that the curves that depict the temporal changes in the flow rate and saturation converge upon increase of the matrix size (i.e. the distance between the curves gradually decreases).

The values of the capillary pressure can still be well predicted by equation (32), see e.g. figure 16 where the pressure profiles in a matrix with 3×3 elements are shown.

Figure 17 depicts the temporal changes in the capillary pressure during the liquid/liquid displacement in all larger matrices. The number of the bumps during the stage when the meniscus still remains within the matrix is equal to the number of the vertical elements in a matrix. The amplitude of the bumps becomes smaller upon addition of the elements to the matrix. One may also observe the convergence of the capillary pressure curves, so that the distance between the curves become gradually smaller upon the increase of the number of the elements in the matrix. In particular, the calculations fulfilled for the matrix with the 6×6 structuring elements give already the accurate prediction of the level of the capillary pressure in a porous medium.

5. Conclusions

We develop a very detailed description for the immiscible liquid/liquid displacement through a uniform network of capillaries that we use as a rough representation of a micro-volume of a porous medium. The numerical modelling is based on the phase-field approach. The governing equations are solved in primitive variables, in terms of pressure and velocity. The calculations are run using modern GPUs. The major focus of our study is the calculation of the dynamic capillary pressure for a volume of the porous medium.

The calculations are performed for a single capillary and for 2D networks of capillaries of different sizes. We found that, qualitatively, for all considered geometries, the liquid/liquid displacement always undergoes the same set of particular stages: (i) right after the moment of turning on the pressure difference between the ends of the matrix, the liquid/liquid menisci experience a number of capillary oscillations; the magnitude of the oscillations is controlled by

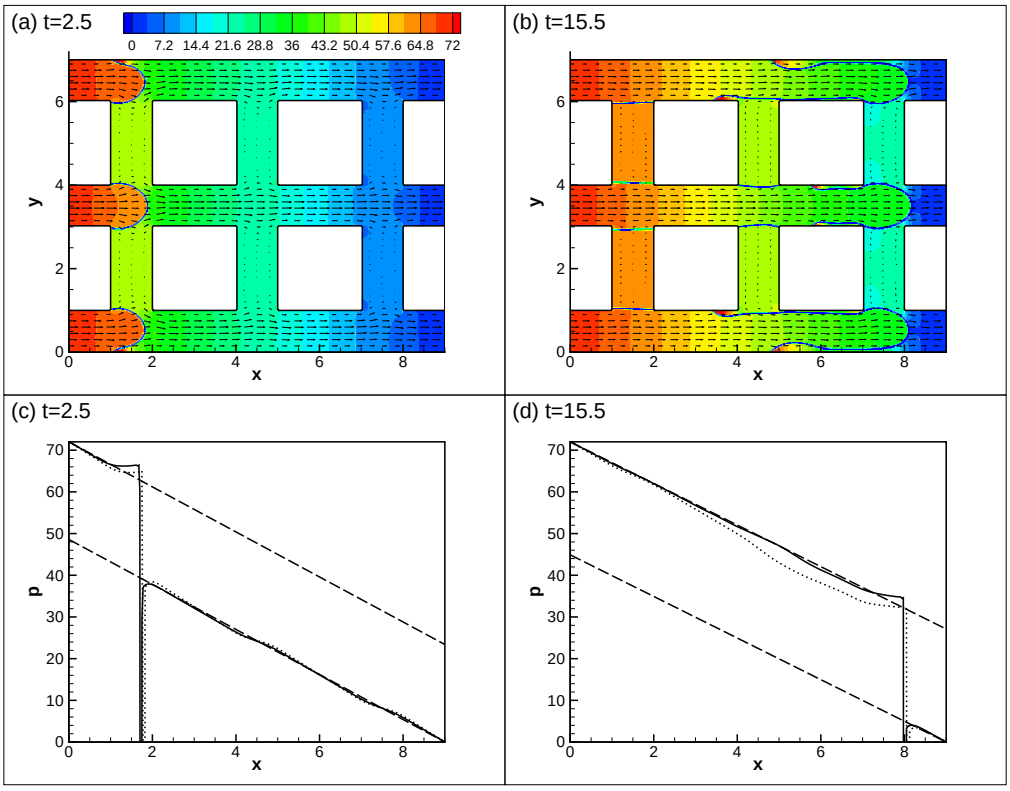

Figure 16: (a,b) The fields of pressure (isolines) and velocity (arrows) for a matrix with 3×3 elements. (c,d) The pressure profiles along the capillary for different vertical positions. The dashed lines depict the lines, $p_1 - (p_1 - p_c)x/L_x$ and $-(p_1 - p_c)(x - L_x)/L_x$, with $p_c = 17.6$ in (c), and $p_c = 15.3$ in (d), respectively. The data are obtained for $Cn = 4 \cdot 10^{-4}$, $M = 2.5 \cdot 10^{-4}$, $Re = 1$, and $Pe = 10^4$. The pressure difference between the ends of the capillary is $p_1 = 8L_x/Re = 48$.

the surface tension coefficient and by the Peclet number; the resolution of these short-term quick oscillations turns out to be one of the major difficulties of the numerical simulations; (ii) later, the meniscus's shape is set and the piston-like propagation of the displacement front through the matrix can be observed; (iii) when the menisci reach the outlet end of the matrix (the break-through time), some volumes of the displacing liquid still remain on the walls of the matrix; so further pumping of the displacing fluid results in scratching of these remainders from the walls; (iv) finally, the steady stage is reached when the displaced fluid however still remains within some elements of the matrix, although the further pumping of the displacing liquid does not lead to any differences in distribution of the liquids within the matrix. We also showed that the Peclet number defines the speed of sliding of the contact line along the walls.

We demonstrate that all integral parameters (including the capillary pressure) that characterise the liquid/liquid displacement within the matrices of different sizes converge to some limiting curves, indicating that the matrix with the size less than 10×10 elements is sufficient to give the accurate prediction of the capillary pressure in a homogeneous porous medium. We also demonstrate that the capillary pressure in a matrix can be accurately predicted from a simple formula $p_c = (1 - Q_2/Q_1)(p_1 - p_2)$, which relates the capillary pressure to the ratio of the flow rates for the two-phase (Q_2) and single-phase (Q_1) fluid flows. The level of the capillary pressure determined in our study will obviously vary with the change of the governing parameters, with the change of the surface tension coefficient, wetting properties, and geometry of the solid matrix. The goal of the present study was to illustrate how the capillary pressure for a two-phase flow in a porous medium can be calculated on the basis of the direct hydrodynamic simulations. In the future, the calculations fulfilled in this work can be conducted for other values of the parameters to establish the dependencies of the capillary pressure on various physical effects (similar to the Leverett formula).

The accurate modelling of a two-phase flow in uniform matrices is important for detailed understanding of the capillary properties of complex interfaces, and for experimental verification of the theoretical concepts using synthetic porous matrices.

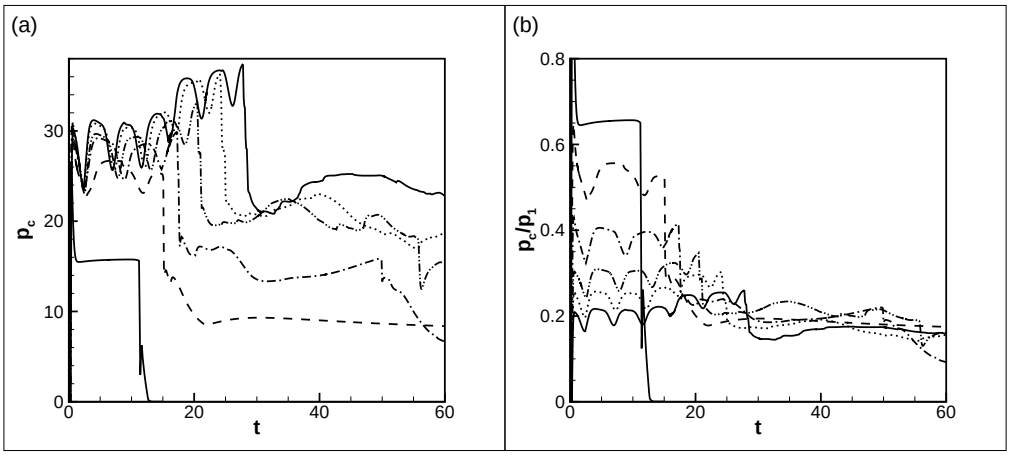

Figure 17: The capillary pressure (a) and the capillary pressure relative to the pressure difference between the ends of the matrix (b). The data are obtained for $Cn = 10^{-4}$, $M = 2.5 \cdot 10^{-4}$, $Re = 1$ and $Pe = 10^4$. The results are shown for a single tube (shorter solid lines) and for the matrices with 2×2 (dashed lines), 3×3 (dash-dotted lines), 4×4 (dash-dot-dotted lines), 5×5 (dotted lines), and 6×6 (solid lines) elements.

It should be also noted that uniform matrices, considered in this study, are obviously insufficient for a realistic representation of all features (e.g. heterogeneity) of the real (e.g. geological) porous medium. Direct modelling of interfaces accounting for the surface tension in large non-uniform matrices becomes, however, a too computationally-demanding task. For instance, to replicate the pore scale heterogeneity using pore/throat size distributions of real rock samples is necessary to have a large enough domain to encompass the spatially correlated features of porous medium. For example for modelling of sandstone, the mean of the distances between the centres of the pore bodies should agree with Berea sandstone with the characteristic length of 100 to 150 μm (Oren and Bakke, 2003). The network of a similar size should already include more than a million of elements. We envisage that a realistic approach would be the combination of the direct modelling with the Darcy-based theory: the accurate calculations of the phenomenological parameters for a micro-level that is represented by a uniform matrix, and then averaging of the results with the use of the Darcy approach for a larger heterogeneous volume built up from the micro-matrices of different sizes and properties.

6. Acknowledgements

This research work is partially financially supported by the Russian Foundation for Basic Research (grant 18-01-00782). The authors acknowledge the use of the IRIDIS High Performance Computing Facility, and associated support services at the University of Southampton, in the completion of this work.

References

Ahmadlouydarab, M., Feng, J.J., 2014. Motion and coalescence of sessile drops driven by substrate wetting gradient and external flow. J. Fluid Mech. 746, 214–235.

Aker, E., Maloy, K.J., Hansen, A., Batrouni, G.G., 1998. A two-dimensional network simulator for two-phase flow in porous media. Transp. Porous Media 32, 163–186.

Barenblatt, G.I., Patzek, T.W., Silin, D.B., 2003. The mathematical model of nonequilibrium effects in water-oil displacement. SPE Journal , 87329.

Barley, J., Ruth, D., 2001. Relative permeability analysis of tube bundle models, including capillary pressure. Transport in Porous Media 45, 447–480.

Cahn, J.W., Hilliard, J.E., 1959. Free energy of a nonuniform system. iii. nucleation in a two-component incompressible fluid. J. Chem. Phys. 31, 688–699.

Ding, H., Spelt, P.D.M., Shu, C., 2007. Diffuse interface model for incompressible two-phase flows with large density ratios. Journal of Computational Physics 226, 2078–2095.

Ferziger, J.H., Peric, M., 2002. Computational Methods for Fluid Dynamics. Springer.

de Gennes, P.G., Brochard-Wyart, F., Quere, D., 2004. Capillarity and Wetting Phenomena: Drops, Bubbles, Pearls, Waves. Springer.

Gray, W., Hassanizadeh, S., 1998. Macroscale continuum mechanics for multiphase porous-media flow including phases, interfaces, common lines and common points. Advances in Water Resources 21, 261–281.

Guermond, J.L., Minev, P., Shen, J., 2006. An overview of projection methods for incompressible flows. Computer methods in applied mechanics and engineering 195, 44–47.

Harris, M., 2019. Optimizing parallel reduction in cuda. https://developer.download.nvidia.com/assets/cuda/files/reduction.pdf. [Online; accessed 20-December-2019].

Hassanizadeh, S., Gray, W., 1993. Thermodynamic basis of capillary pressure in porous media. Water Resources Research 29, 3389–3405.

Hornug, U., 1997. Homogenization and Porous Media. Springer.

Huang, H., Meakin, P., Liu, M., 2005. Computer simulation of two-phase immiscible fluid motion in unsaturated complex fractures using a volume of fluid method. Water Resources Research 41, W12413.

Jacqmin, D., 1999. Calculation of two-phase navier-stokes flows using phase-field modeling. Journal of Computational Physics 155, 96–127.

Jacqmin, D., 2000. Contact-line dynamics of a diffuse fluid interface. J. Fluid Mech. 402, 57–88.

Jespersen, D.C., 2010. Acceleration of a cfd code with a gpu. Scientific Programming 18, 193–201.

Kafka, F.Y., Dussan V., E.B., 1979. On the interpretation of dynamic contact angles in capillaries. J. Fluid Mech. 95, 639–666.

Khaz'ali, A., Moghadasi, J., 2019. Capillary-dominated two-phase flow modeling in porous media using starfish. Journal of Petroleum Exploration and Production Technology 9, 1211–1223.

Kheniene, A., Vorobev, A., 2013. Capillary behaviour in porous solids. Phys. Rev. E 88, 022404.

Landau, L.D., Lifshitz, E.M., 1987. Fluid Mechanics. Volume 6 of the Course of Theoretical Physics. Elsevier.

Leverett, M.C., 1941. Capillary behaviour in porous solids. Transactions of the AIME 142, 159–172.

Li, K., Shen, P., Qing, T., 1994. A new method for calculating oil-water relative permeabilities with consideration of capillary pressure. Mechanics and Practice 16, 46–52.

Lowengrub, J., Truskinovsky, L., 1998. Quasi-incompressible cahn-hilliard fluids and topological transitions. Proc. R. Soc. London, Ser. A 454, 2617–2654.

McClure, J., Armstrong, R., Berrill, M., Schluter, S., Berg, S., Gray, W., Miller, C., 2018. Geometric state function for two-fluid flow in porous media. Physical Review Fluids 3, 084306.

Ngan, C.G., Dussan V., E.B., 1982. On the nature of the dynamic contact angle: an experimental study. J. Fluid Mech. 118, 27–40.

Niessner, J., Berg, S., Hassanizadeh, S.M., 2011. Comparison of two-phase darcy's law with a thermodynamically consistent approach. Transport in porous media 88, 133–148.

Nordbotten, J., Celia, M., Dahle, H., Hassanizadeh, S., 2008. On the definition of macroscopic pressure for multiphase flow in porous media. Water Resources Research 44, W06S02.

Oren, P.E., Bakke, S., 2003. Reconstruction of berea sandstone and pore-scale modelling of wettability effects. Journal of Petroleum Science and Engineering 39, 177–199.

Papatzacos, P., 2002. Macroscopic two-phase flow in porous media assuming the diffuse-interface model at pore level. Transport in Porous Media 49, 139–174.

Prodanovic, M., Bryant, S.L., 2006. A level set method for determining critical curvatures for drainage and imbibition. J. Colloid Interface Sci. 304, 442–458.

Prokopev, S., Vorobev, A., Lyubimova, T., 2019. Phase-field modeling of an immiscible liquid-liquid displacement in a capillary. Phys. Rev. E 99, 033113.

Raeini, A., Bijeljic, B., Blunt, M., 2018. Generalized network modeling of capillary-dominated two-phase flow. Physical Review E 97, 023308.

Raeini, A., Blunt, M., Bijeljic, B., 2012. Modelling two-phase flow in porous media at the pore scale using the volume-of-fluid method. Journal of Computational Physics 231, 5653–5668.

Sanders, J., Kandrot, E., 2010. CUDA by Example: An Introduction to General-Purpose GPU Programming. Addison-Wesley Professional.

Shams, M., Raeini, A., Blunt, M., Bijeljic, B., 2018. A numerical model of two-phase flow at the micro-scale using the volume-of-fluid method. Journal of Computational Physics 357, 159–182.

Thibault, J.C., Senocak, I., 2009. Cuda implementation of a navier-stokes solver on multi-gpu desktop platforms for incompressible flows, in: 47th AIAA Aerospace Sciences Meeting Including The New Horizons Forum and Aerospace Exposition 5 - 8 January 2009, Orlando, Florida, American Institute of Aeronautics and Astronautics.

Vorobev, A., 2010. Boussinesq approximation of the cahn-hilliard-navier-stokes equations. Phys. Rev. E 82, 056312.

Vorobev, A., 2014. Dissolution dynamics of miscible liquid/liquid interfaces. Curr. Opin. Colloid Interface Sci. 19, 300–308.

Vorobev, A., Lyubimova, T., 2019. Vibrational convection in a heterogeneous binary mixture. part 1. time-averaged equations. J. Fluid Mech. 870, 543–562.

Wang, Y., Do-Duang, M., Amberg, G., 2016. Viscoelastic droplet dynamics in a y-shaped capillary channel. Phys. Fluids 28, 033103.

Washburn, E.W., 1921. The dynamics of capillary flow. Proceedings of the Royal Society A 17, 273–283.

Wooding, R.A., Morel-Seytoux, H.J., 1976. Multiphase fluid flow through porous media. Annu. Rev. Fluid Mech. 8, 233–274.